Hydrologic controls on seasonal and inter-annual variability of Congo River particulate organic matter source and reservoir age

Jordon D. Hemingway[a,b,*,†], Enno Schefuß[c], Robert G.M. Spencer[d], Bienvenu Jean Dinga[e], Timothy I. Eglinton[f], Cameron McIntyre[f,g,‡], Valier V. Galy[a]

[a]Department of Marine Chemistry and Geochemistry, Woods Hole Oceanographic Institution, 266 Woods Hole Road, Woods Hole, MA 02543, USA

[b]Massachusetts Institute of Technology-Woods Hole Oceanographic Institution Joint Program in Oceanography and Applied Ocean Science and Engineering, 77 Massachusetts Avenue, Cambridge, MA 02139, USA

[c]MARUM – Center for Marine Environmental Sciences, University of Bremen, 28334 Bremen, Germany

[d]Department of Earth, Ocean, and Atmospheric Science, Florida State University, 600 West College Avenue, Tallahassee, FL 32306, USA

[e]Institute de Recherche en Sciences Exactes et Naturelles (IRSEN), Ministere de la Recherche Scientifique, Brazzaville, Congo

[f]Geological Institute, ETH Zürich, Sonneggstrasse 5, 8092 Zürich, Switzerland

[g]Laboratory of Ion Beam Physics, ETH Zürich, Otto-Stern-Weg 5, 8093 Zürich, Switzerland

[*]Corresponding Author. Tel.: +1 508 289 2821. E-mail address: jordon_hemingway@fas.harvard.edu (J.D. Hemingway)

[†]Current Address: Department of Earth and Planetary Sciences, Harvard University, 20 Oxford Street, Cambridge, MA 02138, USA

[‡]Current Address: Scottish Universities Environmental Research Centre, East Kilbride, G750QF, UK

Abstract

We present dissolved organic carbon (DOC) concentrations, particulate organic matter (POM) composition ($\delta^{13}C$, $\delta^{15}N$, $\Delta^{14}C$, N/C), and particulate glycerol dialkyl glycerol tetraether (GDGT) distributions from a 34-month time-series near the mouth of the Congo River. An end-member mixing model using $\delta^{13}C$ and N/C indicates that exported POM is consistently dominated by C_3 rainforest soil sources, with increasing contribution from C_3 vegetation and decreasing contribution from phytoplankton at high discharge. Large C_4 inputs are never observed despite covering ≈ 13 % of the catchment. Low and variable $\Delta^{14}C$ values during 2011 [annual mean = (-148 ± 82) ‰], when discharge from left-bank tributaries located in the southern hemisphere reached record lows, likely reflect a bias toward pre-aged POM derived from the Cuvette Congolaise swamp forest. In contrast, $\Delta^{14}C$ values were stable near -50 ‰ between January and June 2013, when left-bank discharge was highest. We suggest that headwater POM is replaced and/or diluted by C_3 vegetation and pre-aged soils during transit through the Cuvette Congolaise, whereas left-bank tributaries export significantly less pre-aged material. GDGT distributions provide further evidence for seasonal and inter-annual variability in soil provenance. The cyclization of branched tetraethers and the GDGT-0 to crenarchaeol ratio are positively correlated with discharge ($r \geq 0.70$; p-value $\leq 4.3\times10^{-5}$) due to the incorporation of swamp-forest soils when discharge from right-bank tributaries located in the northern hemisphere is high. Both metrics reach record lows during 2013, supporting our interpretation of increased left-bank contribution at this time. We conclude that hydrologic variability is a major control of POM provenance in the Congo River Basin and that tropical wetlands can be a significant POM source despite their small geographic coverage.

Keywords: Biomarkers; Congo River; GDGTs; Particulate Organic Matter; Radiocarbon

1. Introduction

River networks are a major link between terrestrial and aquatic ecosystems and export a large amount of organic carbon (OC) to the coastal ocean (Schlünz and Schneider, 2000). There has thus been a significant effort to determine the geologic and climatic controls on the source, composition, and export flux of particulate OC (POC) in global rivers (Galy et al., 2015; Ludwig et al., 1996). Furthermore, rivers are generally not passive conduits to the ocean, but rather integrate, process, and remineralize multiple sources of terrestrial and aquatic organic matter (OM) during transit (Aufdenkampe et al., 2011; Cole et al., 2007). Although riverine signals are typically interpreted to reflect a catchment-integrated signal, downstream replacement and/or dilution of headwater POC has been observed in many large basins including the Amazon (Hedges et al., 1986; 2000), Ganges-Brahmaputra (Galy et al. 2008; 2011), and Orange (Herrmann et al., 2016) Rivers. Discerning the controls on POC overprinting is therefore critical in order to accurately assess the ability of rivers to integrate terrestrial signals throughout their catchments.

Specific to the Congo Basin, recent studies using dissolved lithium and silicon isotopes indicate that "black water" tributaries draining the permanently waterlogged Cuvette Congolaise swamp forest (Figure 1a; Keddy et al., 2009) contribute 20 to 60 % of water discharged at Brazzaville/Kinshasa depending on the season (Cardinal et al., 2010; Henchiri et al., 2016). However, the contribution of this end-member to exported particulate OM (POM) remains unknown (Spencer et al., 2016). Still, it has been shown that carbon-rich, inter-fluvial peat deposits within the Cuvette Congolaise are ombrotrophic (*i.e.* rainwater-fed), implying that seasonal drainage of these regions is a net source of local OM to the river network (Dargie et al., 2017; Lee et al., 2011). This is supported by the stable carbon isotope and molecular composition of exported plant-wax lipids, which are consistently dominated by a swamp-forest-derived C_3 signal during periods of high discharge (Hemingway et al., 2016). Furthermore, millennial-scale climatic and hydrologic variability has likely influenced the ability of the Cuvette Congolaise to act as an OM reservoir and a POM source. For example, the terrestrial reservoir age of exported plant wax lipids has been steadily increasing since the humid Early- to Mid-Holocene (≈ 10,000 to 5,000 yr bp), suggesting that remobilization of pre-aged, Cuvette-derived OM becomes more apparent as rainfall within the basin decreases (Schefuß et al., 2016).

Despite these findings, quantitatively partitioning POM sources and understanding the mechanisms that control their variability on seasonal to inter-annual timescales remains an open question in the Congo River Basin. To estimate POM source contributions, multiple (pseudo) conservative tracers such as $\delta^{13}C$, $\Delta^{14}C$, and the particulate total nitrogen (TN) to POC ratio (written N/C) are frequently used in end-member mixing models (Hilton et al., 2010; Hossler and Bauer, 2012; Perdue and Koprivnjak, 2007). However, this requires that end-member compositions are well-constrained and can lead to spurious results if temporal variability in such composition is unknown.

In addition to bulk measurements, microbial glycerol dialkyl glycerol tetraether (GDGT) membrane lipids can provide further constrains on POM source contributions. The molecular compositions of both branched (brGDGTs) and isoprenoid (isoGDGTs) GDGTs have become commonly used proxies for POM provenance and catchment environmental conditions (see Schouten et al., 2013a for review). For example, the methylation of branched tetraether (MBT') and cyclization of branched tetraether (CBT) indices have been shown to co-vary with temperature and pH in a global soil dataset (De Jonge et al., 2014b; Peterse et al., 2012; Weijers et al., 2007) and have thus been used as a tracer for POM source in large fluvial catchments (De Jonge et al., 2014a; Zell et al., 2013). Because the Congo River catchment covers multiple ecosystems that are described by different characteristic environmental conditions including soil pH (Mayaux et al., 2004; Spencer et al., 2012), GDGT signals should provide an additional quantitative tool for POM source partitioning.

POM and GDGT spatiotemporal variability implies that geographic integration in large river systems is not uniform and that relative end-member contributions are subject to large seasonal and inter-annual changes (*e.g.* Galy et al., 2008; Spencer et al., 2016; Zell et al., 2013). To understand this variability in the Congo River Basin, we expand on published records (Bouillon et al., 2012; 2014; Coynel et al., 2005; Hemingway et al., 2016; Mariotti et al., 1991; Marwick et al., 2015; Spencer et al., 2012; 2016) by presenting dissolved organic carbon (DOC) concentrations, POM composition ($\delta^{13}C$, $\delta^{15}N$, $\Delta^{14}C$, N/C), and GDGT distributions from a continuous 34-month time-series collected at Brazzaville/Kinshasa. By comparing our results with those from a two-year record of Oubangui River POM at Bangui Station (Bouillon et al., 2012; 2014) and with campaign-style POM samples (*i.e.* single time point) collected throughout

111 the basin (Marwick et al., 2015; Spencer et al., 2012), we further constrain POM source
112 evolution during transit through the Cuvette Congolaise.
113
114 **2. Study Site**
115 The Congo River drains 3.6×10^6 km^2 of central Africa between 10° N and 15° S and is
116 highly influenced by the seasonal north-to-south migration of the tropical rainbelt (Gasse, 2000).
117 This leads to strong latitudinal gradients in vegetation and ecosystem type (Mayaux et al., 2004),
118 including the permanently waterlogged Cuvette Congolaise swamp forest (Figure 1a), as well as
119 corresponding changes in C_3 vs. C_4 landcover (Figure 1b; Still and Powell, 2010). The Congo
120 Basin is dominated by C_3 closed-canopy evergreen forest near the equator and deciduous
121 woodland/shrubland at the northern and southern peripheries, with smaller contributions by
122 deciduous and montane forests, mosaic savanna/grassland, and swamp forest (Table 1). Recent
123 evidence indicates that inter-fluvial, ombrotrophic basins within the Cuvette Congolaise
124 constitute the most expansive tropical peatland complex on Earth ($\approx 1.45\times10^5$ km^2) and contain
125 approximately 29 % of global tropical peat stocks ($\approx 30.6\times10^9$ tOC; Dargie et al., 2017). In
126 contrast, the Oubangui sub-basin upstream of Bangui Station contains mostly mosaic
127 savannah/grassland and deciduous woodland/shrubland, although this does not appear to result in
128 significant C_4 landcover (12.9 %; Table 1; Still and Powell, 2010).
129 Congo River discharge (Q_w) recorded at Brazzaville/Kinshasa is remarkably stable and
130 predictable, with an annual maximum near 50,000 m^3 s^{-1} and a minimum near 25,000 m^3 s^{-1}
131 (Figure 2a; Coynel et al., 2005; Laraque et al., 2009; Spencer et al., 2014). Increased
132 precipitation in the north of the catchment between May and September (Mahe, 1993) and a ≈ 1
133 to 2 month transit time (Bricquet, 1993) leads to discharge maxima of right-bank tributaries such
134 as the Oubangui River during Nov-Dec-Jan (Bouillon et al., 2012; 2014; Coynel et al., 2005) and
135 corresponds to elevated water flux through the Cuvette Congolaise during this time. Between
136 November and March, southern-hemisphere precipitation increases left-bank tributary
137 contribution in response to the seasonal rainbelt migration and is the source of the secondary
138 discharge maximum observed during Apr-May-Jun (Figure 2a; Bricquet, 1993; Mahe, 1993).
139 Importantly, the largest left-bank tributary (Kasai River) enters the main-stem downstream of the
140 Cuvette Congolaise. In contrast to the Congo River main-stem, Oubangui River discharge is

141 highly seasonal, ranging from ≈ 300 m^3 s^{-1} in Mar-Apr-May to ≈ 9,000 m^3 s^{-1} in Oct-Nov-Dec
142 (Bouillon et al., 2012; 2014).
143
144 **3. Materials and Methods**
145 3.1. Sample collection
146 Congo River samples were collected monthly between November 2010 and August 2013
147 near Brazzaville/Kinshasa, just downstream of the Pool Malebo and ≈ 300 km upstream of the
148 Congo Estuary (Figure 1; Table 1). The sampling location is downstream of all major tributaries,
149 capturing > 95 % of the total catchment (Spencer et al., 2012). Water for total suspended
150 sediments (TSS) was collected from the surface of the river and filtered through 0.22 μm
151 polyether sulfone (PES) membrane filters. After drying (60 °C) and shipment, samples were re-
152 suspended in 18.2 MΩ Milli-Q water, freeze-dried, and weighed for TSS concentration.
153 Simultaneously, water was collected for DOC analysis and filtered through 0.7 μm pre-
154 combusted (550 °C, 4 hours) GF/F filters into acid pre-leached and triple sample-rinsed HDPE
155 bottles. DOC samples were acidified to pH 2 using trace-metal grade HCl and immediately
156 frozen until further analysis.
157 Surface water temperatures (T_{riv}) were measured concurrently using a YSI Professional
158 Plus multiparameter instrument (YSI Incorporated) and daily discharge was measured at a
159 nearby gauging station operated by the Institute de Recherche en Sciences Exactes et Naturelles
160 (Republic of Congo) using a rating curve that is periodically updated by Acoustic Doppler
161 Current Profiler transects. Triplicate transects suggest that river discharge measurements are
162 precise to ± 5 %, although precision is likely lower during high discharge due to overbank
163 flooding (Spencer et al., 2014). Monthly mean air temperature recorded at Brazzaville/Kinshasa
164 (MAT_{Braz}; 4.25° S, 15.25° E) was obtained from the National Oceanic and Atmospheric
165 Administration (NOAA) National Climate Data Center database. MAT was missing for one
166 month (April 2012) and was therefore estimated as the average between mean daily maximum
167 and minimum temperatures during that month.
168
169 3.2. Bulk measurements
170 DOC concentrations (written as [DOC]) were quantified via high-temperature
171 combustion using a Shimadzu TOC-V organic carbon analyzer. Each sample was injected until

there existed triplicate measurements with a coefficient of variability < 2 % and was calibrated to a six-point calibration curve after accounting for instrument drift using an internal control standard (Mann et al., 2012). [DOC] is taken as the mean of these triplicate values with a relative uncertainty (± 1σ) of ± 2 %.

Organic carbon and total nitrogen contents (%OC, %TN) and stable isotope compositions ($\delta^{13}C$, $\delta^{15}N$) were measured on TSS aliquots following the methods of Whiteside et al. (2011). We note that one sample (September 2012) became contaminated by dissolution of the PES membrane during re-suspension and was therefore omitted from bulk measurements. All other samples were fumigated with HCl at 60 °C for 72 hours to remove carbonates prior to %OC and $\delta^{13}C$ measurement using a Fisons elemental analyzer coupled to a Finnigan Delta^{plus} isotope-ratio mass spectrometer (IRMS). %TN and $\delta^{15}N$ measurements were performed similarly but using non-acidified aliquots. All samples were injected in triplicate and calibrated against CO_2 or N_2 gas with known isotope composition. Isotope ratios were validated by analyzing a set of three primary standards (IAEA-N1 ammonium sulfate, USGS-40 glutamic Acid, and glycine) between every ≈ 15 samples and carbon content was further verified using a set of two secondary standards (NBS-19 marble, calcite laboratory standard). Uncertainty is taken as the standard deviation of triplicate measurements and isotope values are reported as per-mille (‰) deviations from Vienna Pee Dee Belemnite (VPDB) for ^{13}C and atmospheric N_2 (AIR) for ^{15}N.

Aliquots for radiocarbon analysis, along with a process blank and a set of two laboratory secondary standards (^{14}C-free coal, Nantucket shelf sediment), were subjected to the acidification treatment described above and were oxidized to CO_2 by baking (850 °C, 5 hours) with ≈ 1 g cupric oxide in evacuated and flame-sealed quartz tubes. CO_2 gas was then distilled cryogenically, transferred to Pyrex tubes, and analyzed for radiocarbon content either using a MIni CArbon DAting System (MICADAS) fitted with a gas-ion source (Ionplus AG) at the Laboratory for Ion Beam Physics, ETH Zürich (Christl et al., 2013) or at the National Ocean Sciences Accelerator Mass Spectrometry facility at WHOI (McNichol et al., 1994). Data are corrected for process blanks and reported following the $\Delta^{14}C$ per-mille (‰) notation of Stuiver and Polach (1977).

3.3. GDGT extraction and purification

Remaining Congo River TSS was extracted at 100 °C for 20 minutes in a microwave accelerated reaction system (MARS, CEM Corporation) in 20 mL of dichloromethane (DCM) and methanol (9:1). Because *n*-alkyl lipid isotopes were also measured on these samples (Hemingway et al., 2016), total lipid extracts were saponified at 70 °C for 2 hours using 0.5 mol L^{-1} KOH in methanol. GDGT distributions reported here represent a combination of core lipids and intact polar phospholipids, as base hydrolysis is known to cleave phosphate-bound head groups (Weijers et al., 2011).

Subsequently, 15 mL of 18.2 MΩ Milli-Q water was added and "base" fractions were liquid-liquid extracted into 5 mL hexane 5 times. HCl was then added drop-wise until pH 2 was reached, and "acid" fractions were extracted using 5 mL hexane and DCM (4:1) until the organic phase was clear (typically 5 times). Acid and base fractions were separated by column chromatography using 1 g of Supelclean amino-propyl silica gel (Supelco Analytical) and the following elution scheme: 4 mL hexane (F1); 7 mL hexane and DCM (4:1, F2); 10 mL DCM and acetone (9:1, F3); 14 mL 2% (w/w) formic acid in DCM (F4); 18 mL DCM and methanol (1:1, F5). Acid and base fractions containing GDGTs (F3) were recombined to ensure maximum recovery. To remove *n*-alcohols, combined F3s were subjected to urea adduction in which 500 µL of urea-saturated methanol was added and solvent was evaporated using a stream of N_2 gas to promote urea recrystallization (repeated three times). Crystals were rinsed three times with 5 mL hexane to remove the "non-adducted" fraction containing GDGTs, which was then stored at 4 °C until analysis. Although the additional handling steps described here likely lower GDGT recovery, results from a recent inter-comparison exercise (Schouten et al., 2013b) indicate that our purification protocol does not impart a significant bias in GDGT distributions as compared to other commonly used methods.

3.4. GDGT detection and analysis

GDGTs were detected on an Agilent 1200 series high-pressure liquid chromatograph coupled to an Agilent LC/MSD SL quadrupole mass spectrometer (HPLC-MS) as initially described by Hopmans et al. (2000). Compounds were ionized using atmospheric-pressure chemical ionization (APCI) and detected on their $[M+H]^+$ ions in selected ion monitoring mode. Chromatographic separation was achieved in normal phase through a Grace Prevail Cyano 3 µm column (150 mm × 2.1 mm). Samples were injected (5 µL) and solvent A [99:1 (v/v)

hexane:isopropanol] was pumped at 0.2 mL min^{-1} isocratically for 5 min, then with a linear gradient for 40 min, reaching 10% solvent B [9:1 (v/v) hexane:isopropanol]. We note that this chromatographic method cannot separate multiple co-eluting compounds such as the six distinct peaks at 1050 *m/z* observed by Becker et al. (2013) and the recently discovered 6-methyl brGDGTs IIa' through IIIc' (see Figure S1 for structures; De Jonge et al., 2013; 2014b). Such co-elution could potentially alter calculated brGDGT metrics, although this effect is likely negligible in our sample set (Discussion S1).

A laboratory working standard was injected at multiple concentrations between every 5 to 10 samples (n = 32) and showed < 10 % variability for all metrics over all concentrations throughout the analysis. Metrics and ratios were calculated based on raw areas (*i.e.* molar ratios), assuming an identical response factor of all isoGDGTs and brGDGTs in accordance with current best practice (Schouten et al., 2013a; 2013b). MBT' and CBT were calculated following Peterse et al. (2012) and Weijers et al. (2007), respectively, according to the equations

$$\mathrm{MBT'} = \frac{\{\mathrm{brIa}\}+\{\mathrm{brIb}\}+\{\mathrm{brIc}\}}{\{\mathrm{brIa}\}+\{\mathrm{brIb}\}+\{\mathrm{brIc}\}+\{\mathrm{brIIa}\}+\{\mathrm{brIIb}\}+\{\mathrm{brIIc}\}+\{\mathrm{brIIIa}\}} \quad (1)$$

and

$$\mathrm{CBT} = -\log\left(\frac{\{\mathrm{brIb}\}+\{\mathrm{brIIb}\}}{\{\mathrm{brIa}\}+\{\mathrm{brIIa}\}}\right), \quad (2)$$

where $\{j\}$ is the area of the $[M+H]^+$ ion for compound j. We note that {brIIa} through {brIIIa} represent the sum of co-eluting 5-methyl and 6-methyl compounds (De Jonge et al., 2014b). Additionally, the GDGT-0/cren was calculated as {GDGT-0}/{cren} following Blaga et al. (2009). All samples were injected in triplicate and metrics are reported as the mean and standard deviation of triplicate measurements.

3.5. Data analysis and model setup

All regressions were performed as ordinary least squares (OLS) and statistical results are reported as Pearson correlation coefficients (r) and significance p-values. Time-series average values are reported as the mean ± 1σ standard deviation about the mean. All data analysis was performed in the Python programming language v.2.7 and ArcGIS for Desktop v.10.3. Quantitative contribution of m end members to bulk POM was determined following optimum

multi-parameter analysis using *m*-1 (pseudo-)conservative tracers, as described in Glover et al. (2011). End-member composition uncertainty was incorporated by *(i)* including a weighting factor for each tracer equal to the range of observed values divided by the average end-member uncertainty and *(ii)* allowing for 1 % deviation in the constraint that fractional contributions sum to unity (Glover et al., 2011). Inclusion of such a weighting factor acts to remove potential biases that could be caused by differences in end-member uncertainty across conservative tracers. Additionally, because phytoplankton $\delta^{13}C$ is known to vary seasonally in the Congo Basin (Bouillon et al., 2014), the composition of this end member was allowed to vary and the model was re-initialized for each time point (Discussion S2). To determine the environmental controls on GDGT metrics, redundancy analysis (RDA) was performed following Legendre and Legendre (1998). To aid in visualizing RDA results, the "site" and "species" scores were scaled symmetrically by the square root of corresponding eigenvalues (*i.e.* "Type III" scaling).

4. Results

All environmental parameters and bulk measurements are reported in Table S1 and all GDGT fractional abundances and calculated metrics are reported in Table S2. Discharge, pH, temperature, and OC concentration time-series results are plotted in Figure 2. Molecular and isotope composition time-series results are plotted in Figure 3.

4.1. Environmental parameters

Congo River discharge recorded at Brazzaville/Kinshasa during the time-series ranged from $(23.2 \pm 1.1) \times 10^3$ m^3 s^{-1} in July 2011 to $(54.6 \pm 2.7) \times 10^3$ m^3 s^{-1} in December 2011 (Figure 2a). Annual average discharge for 2012 and 2013 is near the long-term mean value of 38.8×10^3 m^3 s^{-1} (1977 to 2006 inclusive), whereas the average discharge for 2011 (35.3×10^3 m^3 s^{-1}) is the fifth-lowest in this record (Spencer et al., 2012). Importantly, this is due to a significantly suppressed left-bank discharge maximum during Apr-May-Jun as compared to the 1977 to 2006 mean for these months. In contrast, northern-hemisphere peak discharge (Nov-Dec-Jan) for all years in our time-series is near the long-term average (Figure 2a).

MAT_{Braz} correlates strongly with T_{riv} (Table 2) and both are relatively invariable over the time-series (Figure 2e, 2f). T_{riv} ranges from a minimum of 23.8 °C to a maximum of 31.3 °C [mean = (27.9 ± 1.6) °C]. MAT_{Braz} exhibits similar values, ranging from 23.4 °C to 28.9 °C

[mean = (26.2 ± 1.3) °C]. Both T_{riv} and MAT_{Braz} are uncorrelated with all other environmental parameters, bulk POM measurements, and GDGT metrics. In contrast, pH_{riv} is strongly correlated with Q_w over the 13-month subset of the time-series in which data exist (r = -0.97, p-value = 1.25×10^{-8}; Wang et al., 2013) and ranges from a minimum of 5.7 units to a maximum of 6.7 units (mean = 6.2 ± 0.4; Figure 2b).

4.2. Bulk measurements

4.2.1. DOC and POC concentrations

Congo River [DOC] ranges from 5.1 mg L^{-1} in June 2011 to 14.2 mg L^{-1} in October 2012 [mean = (9.0 ± 2.5) mg L^{-1}; Figure 2c] and exhibits statistically significant correlations with Q_w (positive), $\delta^{15}N$ (negative), N/C (negative), and all GDGT metrics (all positive; Table 2). Although we did not measure sediment grain size directly, previous results indicate that Congo River TSS is comprised of (83 ± 2) % fine-grain (< 63 μm) material (n = 4), and there exists no statistical difference between %OC values of coarse- and fine-grained sediments (Spencer et al. 2012). For the samples analyzed here, POC concentration ([POC]) ranges from a minimum of 0.6 mg L^{-1} in August 2013 to a maximum of 2.6 mg L^{-1} in February 2011 [mean = (1.3 ± 0.4) mg L^{-1}; Figure 2d Hemingway et al., 2016] and is uncorrelated with all environmental parameters, bulk measurements, and GDGT metrics (Table 2).

4.2.2. Stable isotope ($\delta^{13}C$, $\delta^{15}N$) and N/C composition

Congo River POC $\delta^{13}C$ values across the time-series range from -27.6 ‰ VPDB (November to December 2010) to -24.6 ‰ VPDB (February 2013), averaging (-26.4 ± 0.7) ‰ VPDB (Figure 3a). Additionally, $\delta^{13}C$ values exhibit a statistically significant positive relationship with N/C (Table 2). The nitrogen stable isotope composition of Congo River POM is slightly more variable than that of carbon, with $\delta^{15}N$ values ranging from 3.9 ‰ AIR (December 2012 to January 2013) to 8.5 ‰ AIR [August 2011; mean = (6.1 ± 1.1) ‰ AIR; Figure 3b]. $\delta^{15}N$ values display a strong negative correlation with both Q_w and [DOC], as well as weaker correlations with N/C (positive), $\Delta^{14}C$ (negative), MBT', CBT, and GDGT-0/cren (all negative; Table 2). Congo River N/C values range from 0.076 (December 2010) to 0.118 (August 2012) with an average of 0.096 ± 0.010 (Figure 3c). Like $\delta^{15}N$ values, N/C displays a negative correlation with Q_w and [DOC], and is additionally negatively correlated with all GDGT metrics

and positively correlated with $\delta^{13}C$ and $\delta^{15}N$ (Table 2). Temporally, $\delta^{15}N$ is described by a small yet statistically significant secular decrease throughout the time-series (-0.3 ‰ yr^{-1}; Figure 3b), whereas the opposite is true for N/C (0.005 yr^{-1}; Figure 3c).

4.2.3. ^{14}C content

Radiocarbon composition of exported Congo River POC is highly variable, with $\Delta^{14}C$ ranging from -309 ‰ in April 2011 to -33 ‰ in February 2013 [mean = (-105 ± 69) ‰; Figure 3d]. Because $\Delta^{14}C$ is more depleted and variable during 2011 as opposed to 2012 and 2013, there exists a statistically significant positive secular trend throughout the time-series, with an increase of 34.0 ‰ yr^{-1} (Figure 3d). Additionally, $\Delta^{14}C$ displays a slight negative correlation with $\delta^{15}N$ as described above, but is uncorrelated with all other environmental variables, bulk measurements, and GDGT metrics (Table 2).

4.3. GDGT distributions

Homologue brIa is the most abundant brGDGT throughout the time-series, contributing between 73 % and 82 % of total brGDGTs [mean = (77 ± 2) %; Table S2]. Homologues brIIa [mean = (14 ± 1) %] and brIb [mean = (5 ± 1) %] are consistently the second- and third-most abundant branched homologues, respectively. All remaining branched homologues contribute 1 to 2 % of the brGDGT total, with the exception of brIIIc which was not detected in any sample. This leads to an MBT' range of 0.80 to 0.86 (mean = 0.84 ± 0.01; Figure 3e) and a CBT range of 1.00 to 1.32 (mean = 1.15 ± 0.08; Figure 3f). IsoGDGTs are significantly less abundant than branched compounds, with total isoGDGTs (crenarchaeol and GDGT-0 only) comprising between 5 and 10 % of the brGDGT total [mean = (6 ± 1) %]. With the exception of July and August 2013, GDGT-0 is more abundant than crenarchaeol, comprising (60 ± 6) % of isoGDGTs and resulting in a GDGT-0/cren ratio ranging from 0.7 to 2.4 (mean = 1.6 ± 0.4; Figure 3g). All GDGT metrics are positively correlated with each other and exhibit strong positive correlations with Q_w and [DOC], as well as negative correlations with $\delta^{15}N$ and N/C (Table 2). Finally, both CBT and GDGT-0/cren exhibit significant decreasing trends throughout the time-series (-0.04 yr^{-1} and -0.2 yr^{-1}, respectively), mostly driven by sharp decreases during 2013 (Figure 3f, 3g).

5. Discussion

356 5.1. OC fluxes, yield, and the importance of the Cuvette Congolaise

357 Congo River [POC] in our dataset is in good agreement with previously published values
358 from nearby sampling sites (Coynel et al., 2005; Mariotti et al., 1991; Spencer et al., 2012;
359 2016). The time-series mean reported here [(1.3 ± 0.4) mg L^{-1}] is slightly lower than that of
360 Mariotti et al. (1991) from the years 1976 and 1983 [mean = (2.0 ± 0.2) mg L^{-1}, n = 10] and of
361 Coynel et al. (2005) from the years 1990 to 1993 (mean = 1.7 mg L^{-1}, n = 23), but is similar to
362 the recent measurements of Spencer et al. (2012; 2016) [mean = (1.5 ± 0.3) mg L^{-1}, n = 19].

363 Suspended sediment export from the Congo River, both in terms of TSS concentration
364 and yield, is significantly lower than for other large temperate and tropical rivers across the globe
365 (Galy et al., 2015; Ludwig and Probst, 1998). However, TSS exhibit high %OC values leading to
366 [POC] roughly half that of other tropical rivers such as the Amazon (Richey et al., 1990). Using
367 a POC yield at each time point, Y(t), calculated as

368

369 $$\mathrm{Y}(t) = \frac{\mathrm{Q_w}(t) \times [\mathrm{POC}](t)}{\mathrm{A}}, \qquad (3)$$

370

371 where A is catchment area, the average annual yield for our time-series is (0.42 ± 0.004) tC km^{-2}
372 yr^{-1} between November 2010 and August 2013, slightly lower than previously published values
373 of 0.68 tC km^{-2} yr^{-1} (Ludwig et al., 1996) and 0.55 tC km^{-2} yr^{-1} (Coynel et al., 2005; Spencer et
374 al., 2016). Annual POC yield for the entire Congo Basin is greater than that of the Oubangui sub-
375 basin (0.26 tC km^{-2} yr^{-1}) due to the fact that northern-hemisphere summer base-flow conditions
376 lead to reduced Oubangui River POC fluxes (Bouillon et al., 2012).

377 Although most rivers display clear positive, nonlinear relationships between discharge,
378 TSS yield, and POC yield (*i.e.* rating curves), such trends are significantly weaker in the Congo
379 River due to a lack of correlation between Q_w and [POC] (Table 2). This result is at least
380 partially due to hysteresis effects. Highest [POC] is generally observed during the rising limb of
381 the hydrograph (Sep-Oct-Nov) due to the onset of Cuvette Congolaise ombrotrophic wetland
382 flushing (Lee et al., 2011), whereas the falling limb (Dec-Jan-Feb) exhibits lower [POC] for
383 similar discharge values (Spencer et al., 2016). Furthermore, during boreal spring and summer
384 when water flux through this region is low and non-erosive (Bricquet, 1993; Henchiri et al.,
385 2016), Cuvette Congolaise wetlands begin to fill and act as water and sediment sink (Lee et al.,
386 2011).

In contrast to POC, Congo River DOC follows typical rating curve behavior due to the positive correlation between Q_w and [DOC] ($r = 0.88$, p-value $= 2.20 \times 10^{-11}$, $n = 34$; Table 2), as has been reported previously (Coynel et al., 2005; Spencer et al., 2016; Wang et al., 2013). Still, [DOC] does display a slight hysteresis effect, with highest concentrations observed during the rising limb of the hydrograph (Sep-Oct-Nov). This result is again due to flushing of Cuvette-derived DOC at this time, as swamp-forest tributaries within the Congo Basin have been shown to reach [DOC] values as high as ≈ 80 mg L^{-1} (Mann et al., 2014). Resulting DOC yield over the course of our time-series is (3.11 ± 0.03) tC km^{-2} yr^{-1}, leading to a dissolved-phase contribution to total exported OC of (87 ± 5) %. Annual DOC yield calculated here is within the range of previously reported estimates (3.44 tC km^{-2} yr^{-1}, Coynel et al., 2005; 2.47 tC km^{-2} yr^{-1}, Ludwig et al., 1996; 3.48 tC km^{-2} yr^{-1}, Spencer et al., 2016), and is roughly double that of the Oubangui sub-basin (1.43 tC km^{-2} yr^{-1}, Bouillon et al., 2012).

5.2. Congo River POM sources: Insight from bulk measurements

Like concentration and flux results, Congo River POM isotope and N/C composition presented here agrees with previously published values from nearby sampling sites (Mariotti et al., 1991; Spencer et al., 2012, 2016). Although our results represent OM contained in bulk TSS, they are nearly identical to published results from the fine fraction only (< 63 μm), as this fraction contains > 80 % of total POM (Spencer et al., 2012). In contrast, coarse material (≥ 63 μm) has been shown to display significantly lower N/C ratios (Figure 4a), as well as higher $\Delta^{14}C$ values (> 0 ‰; Figure 4b) due to incorporation of bomb-derived ^{14}C, and has been interpreted to represent recently fixed rainforest vegetation and plant debris (Spencer et al., 2012).

Generally, Congo River main-stem POM is more enriched in ^{13}C and depleted in N/C relative to the Oubangui River during similar discharge regimes (Figure 5a, 5b; Bouillon et al., 2012; 2014) and plots within the C_3 rainforest end-member range (Table 3; Figure 4a; see Discussion S2 for end-member compositions). This suggests that headwater material is diluted and/or replaced during transit through the Cuvette Congolaise. Although it is likely that both dilution and replacement are occurring simultaneously, we note that we cannot quantitatively separate the importance of these processes given the current dataset. Quantifying the fraction of headwater POM that is remineralized during transit therefore remains an open question in the Congo Basin.

418 Furthermore, predominantly C_4-savanna-derived POM is never observed (Figure 4a)
419 despite large regions of C_4 landcover, especially in southern-hemisphere tributaries (Table 1;
420 Figure 1b). This agrees with the carbon stable isotope composition of plant-wax *n*-alcohols and
421 *n*-alkanoic acids (Hemingway et al., 2016) as well as the molecular composition of lignin
422 phenols (Spencer et al, 2016) extracted from Congo River TSS, which preclude significant C_4-
423 grass inputs to these biomarker classes. However, left-bank tributaries such as the Kasai River
424 exhibit the highest TSS yield for major tributaries within the Congo Basin (Laraque et al., 2009).
425 High yield suggests that a non-negligible fraction of exported POM can be derived from this
426 region, except during 2011 when southern-hemisphere discharge was anomalously low (Figure
427 2a). The lack of significant C_4 contribution observed throughout our time-series is likely due to a
428 combination of low connectivity between distal C_4-dominated regions and the main-stem river
429 channel (Figure 1), as well as dampening of the hinterland signal by C_3-dominated riparian zones
430 (Bouillon et al., 2012). However, we note that, in contrast to other signals, ^{13}C-enriched C_{33} and
431 C_{35} *n*-alkanes have been observed in the Congo River, indicating that distal C_4 inputs to these
432 recalcitrant biomarkers can persist (Hemingway et al., 2016).
433 Significant erosion of rock-derived or "petrogenic" OC (OC_{petro}) in the Congo Basin is
434 unlikely due to its low catchment relief and lack of OC-rich bedrock lithology (Copard et al.,
435 2007). We therefore omit C_4-savanna and OC_{petro} sources form our mixing model and
436 quantitatively calculate the contributions of C_3 tropical rainforest vegetation, C_3 tropical
437 rainforest soils, and autochthonous phytoplankton to Congo River (Spencer et al., 2016; this
438 study) and Oubangui River POM (Bouillon et al., 2012; 2014). We retain δ^{13}C and N/C as
439 conservative tracers since the ^{14}C content of eroded soil is highly variable and difficult to
440 constrain *a priori* and absolute δ^{15}N values of vegetation, soils, and phytoplankton are influenced
441 by unknown nitrogen sources, fixation pathways, and (re)cycling (Kendall et al., 2001; Martinelli
442 et al., 1999). Resulting estimated end-member contributions are reported in Table S3.
443
444 *5.2.1. Seasonal source variability*
445 Congo River POM at Brazzaville/Kinshasa is consistently dominated by C_3-soil-derived
446 material (median = 87 %, inter-quartile range = 80 % to 91 %; Figure 6a), with low contribution
447 by chemically unaltered C_3 vegetation (median = 1 %, inter-quartile range = 0 % to 13 %; Figure
448 6b) and autochthonous phytoplankton production (median = 8 %, inter-quartile range = 6 % to

11 %; Figure 6c). In contrast, Oubangui River POM is composed almost entirely of C_3 rainforest soils when discharge is high (median = 33 %, inter-quartile range = 8 % to 86 %; Figure 6a) and phytoplankton sources during base-flow conditions (median = 62 %, inter-quartile range = 11 % to 92 %; Figure 6c), with minimal contribution by C_3 vegetation throughout the hydrograph (median = 0 %, inter-quartile range = 0 % to 2 %; Figure 6b).

The seasonal importance of phytoplankton-derived POM in the Oubangui River therefore does not propagate to the main-stem Congo River at Brazzaville/Kinshasa due to a combination of: *(i)* dilution by downstream inputs, *(ii)* remineralization during transit, and/or *(iii)* loss due to particle settling and trapping during transit. However, while low throughout the time-series, phytoplankton contribution to Congo River POM does display a statistically significant decrease with increasing discharge (r = -0.60, p-value = 6.10×10^{-6}, n = 48; Figure 6c). This result agrees with observed seasonal trends in C_{24} *n*-alcohol stable carbon isotope composition, as this compound has been shown to be influenced by autochthonous production (Hemingway et al., 2016).

Unlike phytoplankton, contribution by C_3 vegetation to POM is typically higher in the Congo River main-stem than in the Oubangui River and is positively correlated with discharge (r = 0.57, p-value = 1.98×10^{-5}, n = 48; Figure 6b), reflecting increasing admixture of less degraded vascular plant material when water flux through the Cuvette Congolaise is high. Importantly, this end member likely includes any eroded peat material, as such OM has been minimally altered during storage under anoxic conditions and thus retains the $\delta^{13}C$ and N/C signatures of recently fixed rainforest vegetation. Although absolute end-member $\delta^{15}N$ values are difficult to constrain *a priori*, a compilation of tropical rainforest samples indicates that fresh vegetation is depleted in ^{15}N by 6.9 ± 4.5 ‰ relative to soils (Martinelli et al., 1999). In contrast, $\delta^{15}N$ of Oubangui River POM is constant across the hydrograph (Figure 5c) and suggests that this tracer is insensitive to phytoplankton vs. C_3-soil inputs in this system. However, we note that Congo River POM end-member compositions are likely not identical to those in the Oubangui. Still, the strong negative correlation between Congo River POM $\delta^{15}N$ and discharge observed here (Figure 5c) provides further evidence for an increase in chemically unaltered vascular plant material with increasing discharge. This result is additionally supported by observed seasonal variability in the chemical composition and carbon-normalized yield of particulate lignin

phenols, which shift toward higher yield and less degraded signatures when discharge is high (Spencer et al., 2016).

5.2.2. Controls on POC $\Delta^{14}C$

Although consistently dominated by C_3-soil material, the radiocarbon composition of exported Congo River POC is highly variable. Because observed $\Delta^{14}C$ values cannot be explained by OC_{petro} inputs (Copard et al., 2007), we interpret this signal to reflect incorporation of variably-aged biospheric OM. Eroded POC exhibits low and variable $\Delta^{14}C$ values during 2011 [annual mean = (-148 ± 82) ‰] as compared to 2012 [annual mean = (-74 ± 35) ‰] and 2013 [Jan-Aug mean = (-72 ± 41) ‰], suggesting that anomalously low southern-hemisphere discharge in 2011 resulted in an apparent bias toward export of pre-aged, Cuvette-derived soils at this time.

To verify that ^{14}C-depleted POC is indeed sourced from the Cuvette Congolaise, we measured a single POM sample collected from the Sangha River upstream of the Cuvette (2.00º N, 16.08º E) and the Oubangui River within the Cuvette (1.62º N, 18.08º E; Figure 1). By additionally comparing to upstream main-stem samples (Marwick et al., 2015), we are able to characterize the POM composition of all major inputs to the Cuvette Congolaise (Figure 1, white markers; Figure 4). Upstream $\Delta^{14}C$ values are significantly higher than those from our time-series and are similar to results from ≥ 63 μm POC (Marwick et al., 2015; Spencer et al., 2012), suggesting that main-stem headwater POM is dominated by recently fixed C_3 vegetation. In contrast, both the Sangha and Oubangui $\Delta^{14}C$ values are within the range of our main-stem time-series (Figure 4b), although the Oubangui River sample is significantly more depleted in ^{14}C relative to that from the Sangha River. Because this Oubangui River sampling location is located within the Cuvette Congolaise (Figure 1), this result supports our interpretation that Cuvette-derived, ^{14}C-depleted OC overprints headwater material during transit. Furthermore, low $\Delta^{14}C$ values for peat samples collected within the Cuvette Congolaise (Figure 4b; Dargie et al., 2017) provide direct evidence for the existence of ^{14}C-depleted OC in this region. Combined, these results strongly suggest that main-stem POM is dominated by pre-aged material upon exiting the Cuvette Congolaise.

In contrast to 2011, POC $\Delta^{14}C$ values were stable near -50 ‰ from January to June 2013, when left-bank tributary discharge peaked above the 1977 to 2006 average for these months

(Figure 2a). Ecosystems drained by left-bank tributaries in the Congo Basin (grassland, woodland/shrubland, Figure 1a) are highly productive with most biomass produced as leaves and foliage, thus resulting in a large carbon flux into soils (Bloom et al., 2016). Together with warm and wet environmental conditions, this leads to high soil OM turnover and short soil residence times (Carvalhais et al., 2014). Combined with relatively high TSS yields in these tributaries (Laraque et al., 2009), this supports our interpretation that increased precipitation and discharge in the southern area of the basin will lead to higher POC ^{14}C content. Increased left-bank contribution should therefore maintain the predominance of the C_3 soil end member but will dilute any contributions by pre-aged Cuvette Congolaise OM, consistent with $\Delta^{14}C$ and end-member mixing results for 2013 (Figure 3d, 6a).

Increasing terrestrial reservoir ages (*i.e.* lower radiocarbon composition relative to the atmosphere at the time of deposition) since the Early- to Mid-Holocene have been observed in plant-wax lipids, wood pieces, and OC extracted from Congo Fan sediments, concomitant with decreasing precipitation intensity (Schefuß et al., 2005; 2016). This trend has been interpreted to reflect increasing erosion of pre-aged, previously inundated Cuvette Congolaise swamp deposits (Schefuß et al., 2016). These results indicate that Cuvette-derived POM contains eroded soils with lower ^{14}C content than those sourced from other ecosystems within the basin, likely due to efficient OC preservation under permanently inundated, anoxic conditions. The time-series $\Delta^{14}C$ results presented here further support this idea and show that relative changes in Cuvette Congolaise inputs lead to variability in exported POC ^{14}C content on inter-annual in addition to millennial timescales. Thus, if the observed decreases in Apr-May-Jun precipitation in the Congo Basin over the past decade continue (Zhou et al., 2014), our data suggest that exported soil-derived POM will further bias toward pre-aged Cuvette Congolaise sources under future declining discharge regimes.

5.3. Congo River POM sources: Insight from GDGT metrics

Congo River GDGTs can provide additional information regarding POM provenance, especially since variability in material sourced from the highly acidic, anoxic Cuvette Congolaise (Mann et al., 2014) should be reflected in CBT and GDGT-0/cren metrics (Blaga et al., 2009; Weijers et al., 2007). Indeed, these indices display large variability throughout the time-series (Figure 3f, 3g), indicating significant seasonal changes in GDGT source. Although GDGT

distributions for each end member could not be measured directly, redundancy analysis (RDA; Legendre and Legendre, 1998) indicates that a majority of observed discharge and GDGT metric variance load onto the same canonical axis, RDA1 (Figure 7, Table S4). Analogous to bulk POM results, this suggests a hydrologic control on GDGT sources and molecular distributions in Congo River TSS.

It is possible that seasonal variability is due to *in situ* brGDGT production within the river when discharge is low, as this would lead to the observed decreases in MBT' and CBT at this time (Peterse et al., 2009; Tierney et al., 2010) and has previously been invoked to explain brGDGT distributions in other river systems (De Jonge et al., 2014a; Zell et al., 2014). However, significant *in situ* brGDGT production within the water column on seasonal timescales is unlikely, as these compounds have been shown to exhibit much longer growth times. For example, Peterse et al. (2015) observed no *in situ* production of intact polar brGDGTs in 160-day incubations of TSS from New Zealand rivers. Although the incubation conditions of Peterse et al. (2015) are not identical to those within the Congo River, significant autochthonous production would additionally lead to $\delta^{13}C$ and N/C values approaching those of the phytoplankton end-member at low discharge, which is not observed (Figure 5a, 5b).

Rather, variability is likely due to incorporation of GDGTs produced in permanently inundated, anoxic Cuvette Congolaise soils when discharge through this region is high. This is supported by the observation that water-logged, acidic soils in western Uganda exhibit significantly higher CBT values than well-drained, aerobic soils from the same transect (Loomis et al., 2011). Similarly, water-saturated and oxygen-depleted peat bogs have been shown to display higher CBT values than nearby aerobic sites (Huguet et al., 2010), as dissolved oxygen content has been shown to exert a strong control on bacterial community composition (Hansel et al., 2008) and likely brGDGT distributions. In our time-series, flux-weighted-average CBT during 2013 is significantly lower than in 2011 and 2012 (Figure 3f), consistent with elevated southern-hemisphere discharge and increased contribution by left-bank POM in 2013.

Additionally, GDGT-0/cren ratios ≥ 2 are generally thought to represent substantial contribution by anaerobic methanogenic archaea (Blaga et al., 2009). Significant methanogenesis in Cuvette Congolaise soils is indirectly supported by the high concentrations and low $\delta^{13}C$ values of amino-bacteriohopanepolyls in soils of this region (Spencer-Jones et al., 2015; Talbot et al., 2014). Therefore, in addition to higher CBT values, increased incorporation of GDGTs

572 from swamp-forest soils during high discharge should lead to elevated GDGT-0/cren ratios, as is
573 observed (Figure 3g). Similar to CBT, flux-weighted-average GDGT-0/cren is lowest in 2013 as
574 compared to 2011 and 2012, further supporting the idea that increased left-bank contribution is
575 the source of exported POM with younger ^{14}C ages and less acidic/methanogenic GDGT sources
576 at this time. In contrast, low southern-hemisphere discharge in 2011, and to a lesser degree in
577 2012 (Figure 2a), leads to exported POM that is biased toward pre-aged Cuvette Congolaise
578 soils. GDGT metrics therefore agree with bulk end-member mixing-model and $\Delta^{14}C$ results,
579 further highlighting the importance of the Cuvette Congolaise in determining exported POM
580 signals from the Congo River.
581
582 **6. Conclusion**
583 We present a 34-month record of Congo River DOC concentrations, POM composition
584 ($\delta^{13}C$, $\delta^{15}N$, $\Delta^{14}C$, N/C), and GDGT distributions in order to constrain seasonal and inter-annual
585 variability in the source of exported POM. Our results indicate that all Congo River POM
586 samples are consistently dominated by C_3 soil inputs throughout the time-series, with decreasing
587 contribution by phytoplankton and increasing contribution by fresh C_3 vegetation during high
588 discharge. In contrast, large inputs by C_4 grasses are never observed despite their considerable
589 extent within the Congo Basin.
590 Exported POC displays low and variable ^{14}C content, especially during 2011 when
591 southern-hemisphere discharge was anomalously low. Combined with higher CBT and GDGT-
592 0/cren values in 2011, this suggests that pre-aged, acidic, and anoxic Cuvette Congolaise soils
593 are an important source of POM to the Congo River. Furthermore, high southern-hemisphere
594 discharge in spring 2013 coincides with stable, high ^{14}C content and suggests that left-bank
595 tributaries are a source of young soil-derived POM, consistent with lower CBT and GDGT-
596 0/cren at this time.
597 This study demonstrates that POM exported from tropical, wet river catchments can
598 contain significantly pre-aged biospheric material due to protracted storage in anoxic wetland
599 soils. We emphasize that permanently inundated areas such as those present in the Cuvette
600 Congolaise are an important reservoir of both dissolved and particulate OM despite their
601 relatively small landcover extent and could be more significant in determining the role of tropical

rivers in the global carbon cycle than previously thought, especially if future hydrologic regimes favor export and remineralization of this material.

Acknowledgements

We thank Carl Johnson (WHOI), Ekaterina Bulygina (Woods Hole Research Center), Sarah Rosengard (WHOI), Helena Pryer (WHOI), Negar Haghipour (ETH), and Lukas Wacker (ETH) for laboratory assistance. J.D.H. was supported by the NSF Graduate Research Fellowship Program under grant number 2012126152; E.S. was supported by the DFG Research Center/Cluster of Excellence "The Ocean in the Earth System" at MARUM – Center for Environmental Sciences; V.V.G. was partly supported by the US National Science Foundation, grants OCE-0851015 and OCE-0928582; R.G.M.S. was partly supported by the US National Science Foundation, grants OCE-0851101, OCE-1333157, and OCE-1464396; and T.I.E. was partly supported by the Swiss National Science Foundation (SNF Grant No. 200021_140850). This manuscript benefitted from constructive comments by one anonymous reviewer, Brad Rosenheim, and editor Jérôme Gaillardet.

References

Aufdenkampe A. K., Mayorga E., Raymond P., Melack J. M., Doney S. C., Alin S. R., Aalto R. E. and Yoo K. (2011) Riverine coupling of biogeochemical cycles between land, oceans, and atmosphere. *Front. Ecol. Environ*. **9**, 53–60.

Becker K. W., Lipp J. S., Zhu C., Liu X.-L. and Hinrichs K.-U. (2013) An improved method for the analysis of archaeal and bacterial ether core lipids. *Org. Geochem*. **61**, 34–44.

Blaga C. I., Reichart G.-J., Heiri O. and Sinninghe Damsté J. S. (2009) Tetraether membrane lipid distributions in water-column particulate matter and sediments: a study of 47 European lakes along a north–south transect. *J. Paleolimnol*. **41**, 523–540.

Bloom A. A., Exbrayat J. F., van der Velde I. R., Feng L. and Williams M. (2016) The decadal state of the terrestrial carbon cycle: Global retrievals of terrestrial carbon allocation, pools, and residence times. *PNAS* **113**, 1285–1290.

Bouillon S., Yambélé A., Spencer R. G., Gillikin D. P., Hernes P. J., Six J., Merckx R. and Borges A. V. (2012) Organic matter sources, fluxes and greenhouse gas exchange in the Oubangui River (Congo River basin). *Biogeosciences* **9**, 2045–2062.

Bouillon S., Yambélé A., Gillikin D. P., Teodoru C., Darchambeau F., Lambert T. and Borges A. V. (2014) Contrasting biogeochemical characteristics of the Oubangui River and tributaries (Congo River basin). *Sci. Rep*. **4**, 5402.

Bricquet J. P. (1993) Les ecoulements du Congo a Brazzaville et la spatialization des apports. *Grands Bassins Fluviaux*, Paris, 27–38.

Cardinal D., Gaillardet J., Hughes H. J., Opfergelt S. and André L. (2010) Contrasting silicon isotope signatures in rivers from the Congo Basin and the specific behaviour of organic-rich waters. *Geophys. Res. Lett*. **37**, L12403.

Carvalhais, N., Forkel M., Khomik M., Bellarby J., Jung M., Migliavacca M., Mu M., Saatchi S., Santoro M., Thurner M., Weber U., Ahrens B., Beer C., Cescatti A., Randerson J., and Reichstein M. (2014) Global covariation of carbon turnover times with climate in terrestrial ecosystems. *Nature* **514**, 213–217.

Christl M., Vockenhuber C., Kubik P. W., Wacker L., Lachner J., Alfimov V. and Synal H. A. (2013) The ETH Zurich AMS facilities: Performance parameters and reference materials. *Nucl. Instrum Meth. B* **294**, 29–38.

Cleveland C. C. and Liptzin D. (2007) C:N:P stoichiometry in soil: is there a "Redfield ratio" for the microbial biomass? *Biogeochemistry* **85**, 235–252.

Cole J. J., Prairie Y. T., Caraco N. F., McDowell W. H., Tranvik L. J., Striegl R., Duarte C. M., Kortelainen P., Downing J. A., Middelburg J. J. and Melack J. M. (2007) Plumbing the Global Carbon Cycle: Integrating Inland Waters into the Terrestrial Carbon Budget. *Ecosystems* **10**, 172–185.

Copard Y., Amiotte-Suchet P. and Di-Giovanni C. (2007) Storage and release of fossil organic carbon related to weathering of sedimentary rocks. *Earth Planet. Sc. Lett*. **258**, 345–357.

Coynel A., Meybeck M., Seyler P., Etcheber H. and Orange D. (2005) Spatial and seasonal dynamics of total suspended sediment and organic carbon species in the Congo River. *Global Biogeochem. Cy*. **19**, GB4019.

Dargie G. C., Lewis S. L., Lawson I. T., Mitchard E. T. A., Page S. E., Bocko Y. E., and Ifo S. A. (2017) Age, extent and carbon storage of the central Congo Basin peatland complex. *Nature* **542**, 86–90.

De Jonge C., Hopmans E. C., Stadnitskaia A., Rijpstra W. I. C., Hofland R., Tegelaar E. and Sinninghe Damsté J. S. (2013) Identification of novel penta- and hexa-methylated branched glycerol dialkyl glycerol tetraethers in peat using HPLC-MS^2, GC-MS, and GC-SMB-MS. *Org. Geochem*. **54**, 78–82.

De Jonge C., Stadnitskaia A., Hopmans E. C., Cherkashov G., Fedotov A. and Sinninghe Damsté J. S. (2014a) In situ produced branched glycerol dialkyl glycerol tetraethers in suspended particulate matter from the Yenisei River, Eastern Siberia. *Geochim. Cosmochim. Ac*. **125**, 476–491.

De Jonge C., Hopmans E. C., Zell C. I., Kim J.-H., Schouten S. and Sinninghe Damsté J. S. (2014b) Occurrence and abundance of 6-methyl branched glycerol dialkyl glycerol tetraethers in soils: Implications for palaeoclimate reconstruction. *Geochim. Cosmochim. Ac.* **141**, 97–112.

Diefendorf A. F., Mueller K. E., Wing S. L., Koch P. L. and Freeman K. H. (2010) Global patterns in leaf ^{13}C discrimination and implications for studies of past and future climate. *PNAS* **107**, 5738–5743.

Galy V. V., France-Lanord C. and Lartiges B. (2008) Loading and fate of particulate organic carbon from the Himalaya to the Ganga-Brahmaputra delta. *Geochim. Cosmochim. Ac.* **72**, 1767–1787.

Galy V. V., Eglinton T. I., France-Lanord C. and Sylva S. P. (2011) The provenance of vegetation and environmental signatures encoded in vascular plant biomarkers carried by the Ganges-Brahmaputra rivers. *Earth Planet. Sc. Lett*. **304**, 1–12.

Galy V. V., Peucker-Ehrenbrink B. and Eglinton T. I. (2015) Global carbon export from the terrestrial biosphere controlled by erosion. *Nature* **521**, 204–207.

Gasse F. (2000) Hydrological changes in the African tropics since the Last Glacial Maximum. *Quaternary Sci. Rev*. **19**, 189–211.

Glover D. M., Jenkins W. J. and Doney S. C. (2011) Optimum multiparameter (OMP) analysis. In *Modeling Methods for Marine Science*. Cambridge University Press, New York, pp. 86–94.

Graven H. D. (2015) Impact of fossil fuel emissions on atmospheric radiocarbon and various applications of radiocarbon over this century. *PNAS* **112**, 9542–9545.

Hansel C. M., Fendorf S., Jardine P. M. and Francis C. A. (2008) Changes in Bacterial and Archaeal Community Structure and Functional Diversity along a Geochemically Variable Soil Profile. *Appl. Environ. Microb*. **74**, 1620–1633.

Hedges J. I., Clark W. A., Quay P. D., Richey J. E., Devol A. H. and Santos U. de M. (1986) Compositions and fluxes of particulate organic material in the Amazon River. *Limnol. Oceangr*. **31**, 717–738.

Hedges J. I., Mayorga E., Tsamakis E., McClain M. E., Aufdenkampe A. K., Quay P. D., Richey J. E., Benner R., Opsahl S., Black B., Pimintel T., Quintanilla J. and Maurice L. (2000) Organic matter in Bolivian tributaries of the Amazon River: A comparison to the lower mainstream. *Limnol. Oceangr*. **45**, 1449–1466.

Hemingway J. D., Schefuß E., Dinga B. J., Pryer H. and Galy V. V. (2016) Multiple plant-wax compounds record differential sources and ecosystem structure in large river catchments. *Geochim. Cosmochim. Ac*. **184**, 20–40.

Henchiri S., Gaillardet J., Dellinger M., Bouchez J. and Spencer R. G. (2016) Temporal variations of riverine dissolved lithium isotopic signatures unveil contrasting weathering regimes in low-relief Central Africa. *Geophys. Res. Lett*. **43**, GL067711.

Herrmann N., Boom A., Carr A. S., Chase B. M., Granger R., Hahn A., Zabel M., and Schefuß E. (2016) Sources, transport and deposition of terrestrial organic material: A case study from southwestern Africa. *Quat. Sci. Rev*. **149**, 215–229.

Hilton R. G., Galy A., Hovius N., Horng M. J. and Chen H. (2010) The isotopic composition of particulate organic carbon in mountain rivers of Taiwan. *Geochim. Cosmochim. Ac*. **74**, 3164–3181.

Hopmans E. C., Schouten S., Pancost R. D., van der Meer M. T. J. and Sinninghe Damsté J. S. (2000) Analysis of intact tetraether lipids in archaeal cell material and sediments by high performance liquid chromatography/atmospheric pressure chemical ionization mass spectrometry. *Rapid Commun. Mass Sp*. **14**, 585–589.

Hossler K. and Bauer J. E. (2012) Estimation of riverine carbon and organic matter source contributions using time-based isotope mixing models. *J. Geophys. Res*. **117**, G03035.

Huguet A., Fosse C., Laggoun-Défarge F., Toussaint M.-L. and Derenne S. (2010) Occurrence and distribution of glycerol dialkyl glycerol tetraethers in a French peat bog. *Org. Geochem*. **41**, 559–572.

Keddy P. A., Fraser L. H., Solomeshch A. I., Junk W. J., Campbell D. R., Arroyo M. T. and Alho, C. J. (2009) Wet and wonderful: The world's largest wetlands are conservation priorities. *Bioscience* **59**, 39-51.

Kendall C., Silva S. R. and Kelly V. J. (2001) Carbon and nitrogen isotopic compositions of particulate organic matter in four large river systems across the United States. *Hydrol. Process.* **15**, 1301–1346.

Laraque A., Bricquet J. P., Pandi A. and Olivry J. C. (2009) A review of material transport by the Congo River and its tributaries. *Hydrol. Process*. **23**, 3216–3224.

Lee H., Heighley R. E., Alsdorf D., Jung H. C., Shum C. K., Duan J., Guo H., Yamazaki D. and Andreadis K. (2011) Characterizatino of terrestrial water dynamics in the Congo Basin using GRACE and satellite radar altimetry. *Remote Sens. Environ.* **115**, 3530–3538.

Legendre P. and Legendre L. (1998) Canonical alaysis. In *Numerical Ecology*. Elsevier, Amsterdam, pp. 535–636.

Loomis S. E., Russell J. M. and Sinninghe Damsté J. S. (2011) Distributions of branched GDGTs in soils and lake sediments from western Uganda: Implications for a lacustrine paleothermometer. *Org. Geochem*. **42**, 739–751.

738 Ludwig W. and Probst J.-L. (1998) River sediment discharge to the oceans; present-day controls
739 and global budgets. *Am. J. Sci*. **298**, 265–295.
740 Ludwig W., Probst J.-L. and Kempe S. (1996) Predicting the oceanic input of organic carbon by
741 continental erosion. *Global Biogeochem. Cy*. **10**, 23–41.
742 Magill C. R., Ashley G. M. and Freeman K. H. (2013) Ecosystem variability and early human
743 habitats in eastern Africa. *PNAS* **110**, 1167–1174.
744 Mahe (1993) Modulation annuelle et fluctuation interannuelles des precipitations sur le bassin
745 versant du Congo. *Grands Bassins Fluviaux*, Paris, pp. 13–26.
746 Mann P. J., Davydoda A., Zimov N., Spencer R. G. M., Davydov S., Bulygina E., Zimov S. and
747 Holmes R. M. (2012) Controls on the composition and lability of dissolved organic
748 matter in Siberia's Kolyma River. *J. Geophys. Res.-Biogeo*. **117**, 117.G1
749 Mann P. J., Spencer R. G., Dinga B. J., Poulsen J. R., Hernes P. J., Fiske G., Salter M. E., Wang
750 Z. A., Hoering K. A., Six J. and Holmes R. M. (2014) The biogeochemistry of carbon
751 across a gradient of streams and rivers within the Congo Basin. *J. Geophys. Res.-Biogeo*.
752 **119**, 687–702.
753 Mariotti A., Gadel F., Giresse P. and Kinga-Mouzeo (1991) Carbon isotope composition and
754 geochemistry of particulate organic matter in the Congo River (Central Africa):
755 Application to the study of Quaternary sediments off the mouth of the river. *Chem. Geol*.
756 **86**, 345–357.
757 Martinelli L., Piccolo M. C., Townsend A. R., Vitousek P. M., Cueves E., McDowell W. H.,
758 Robertson G. P., Santos O. C. and Treseder K. (1999) Nitrogen stable isotopic
759 composition of leaves and soil: tropical versus temperate forests. *Biogeochemistry* **46**,
760 45–65.
761 Marwick T. R., Tamooh F., Teodoru C. R., Borges A. V., Darchambeau F., and Bouillon, S.
762 (2015) The age of river-transported carbon: a global perspective. *Glob. Biogeochem. Cy.*
763 **29**, 122–137.
764 Mayaux P., Martholomé E., Fritz S. and Belwand A. (2004) A new land-cover map of Africa for
765 the year 2000. *J. Biogeogr*. **31**, 861–877.
766 McNichol A. P., Osborne E. A., Gagnon A. R., Fry B. and Jones G. A. (1994) TIC, TOC, DIC,
767 DOC, PIC, POC—unique aspects in the preparation of oceanographic samples for ^{14}C-
768 AMS. *Nucl. Inst. Methods Phys. Res. B.* **92**, 162-165.

769 Meyers P. A. (1994) Preservation of elemental and isotopic source identification of sedimentary
770 organic matter. *Chem. Geol*. **114**, 289–302.
771 Perdue E. M. and Koprivnjak J.-F. (2007) Using the C/N ratio to estimate terrigenous inputs of
772 organic matter to aquatic environments. *Estuar. Coast. Shelf Sci*. **73**, 65–72.
773 Peterse F., Kim J.-H., Schouten S., Kristensen D. K., Koç N. and Sinninghe Damsté J. S. (2009)
774 Constraints on the application of the MBT/CBT palaeothermometer at high latitude
775 environments (Svalbard, Norway). *Org. Geochem*. **40**, 692–699.
776 Peterse F., van der Meer J., Schouten S., Weijers J. W. H., Fierer N., Jackson R. B., Kim J.-H.
777 and Sinninghe Damsté J. S. (2012) Revised calibration of the MBT–CBT
778 paleotemperature proxy based on branched tetraether membrane lipids in surface soils.
779 *Geochim. Cosmochim. Ac*. **96**, 215–229.
780 Peterse F., Moy C. M. and Eglinton T. I. (2015) A laboratory experiment on the behaviour of
781 soil-derived core and intact polar GDGTs in aquatic environments. *Biogeosciences* **12**,
782 933–943.
783 Powers J. S. and Schlesinger W. H. (2002a) Geographic and vertical patterns of stable carbon
784 isotopes in tropical rain forest soils of Costa Rica. *Geoderma* **109**, 141–160.
785 Powers J. S. and Schlesinger W. H. (2002b) Relationships among soil carbon distributions and
786 biophysical factors at nested spatial scales in rain forests of northeastern Costa Rica.
787 *Geoderma* **109**, 165–190.
788 Rau G. H., Takahashi T. and Marais Des D. J. (1989) Latitudinal variations in plankton $\delta^{13}C$:
789 Implications for CO_2 and productivity in past oceans. *Nature* **341**, 516–518.
790 Richey J. E., Hedges J. I., Devol A. H., Quay P. D., Victoria R., Martinelli L. and Forsberg B. R.
791 (1990) Biogeochemistry of carbon in the Amazon River. *Limnol. Oceangr*. **35**, 352–371.
792 Ross D. J., Tate K. R., Newton P. and Clark H. (2002) Decomposability of C_3 and C_4 grass litter
793 sampled under different concentrations of atmospheric carbon dioxide at a natural CO_2
794 spring. *Plant Soil* **240**, 275–286.
795 Schefuß E., Schouten S. and Schneider R. R. (2005) Climatic controls on central African
796 hydrology during the past 20,000 years. *Nature* **437**, 1003–1006.
797 Schefuß E., Eglinton T. I., Spencer-Jones C. L., Rullkötter J., De Pol-Holz R., Talbot H. M.,
798 Grootes P. M. and Schneider R. R. (2016). Hydrologic control of carbon cycling and
799 aged carbon discharge in the Congo River basin. *Nature Geosci*. **9**, 687–690.

Schlünz, B. and Schneider, R. R. (2000). Transport of terrestrial organic carbon to the oceans by rivers: re-estimating flux-and burial rates. *Int. J. Earth Sci.* **88**, 599-606.

Schouten S., Hopmans E. C. and Sinninghe Damsté J. S. (2013a) The organic geochemistry of glycerol dialkyl glycerol tetraether lipids: A review. *Org. Geochem*. **54**, 19–61.

Schouten S., Hopmans E. C., Rosell-Melé A., Pearson A., Adam P., Bauersachs T., Bard E., Bernasconi S. M., Bianchi T. S., Brocks J. J., Carlson L. T., Castañeda I. S., Derenne S., Selver A. D., Dutta K., Eglinton T. I., Fosse C., Galy V. V., Grice K., Hinrichs K.-U., Huang Y., Huguet A., Huguet C., Hurley S., Ingalls A. E., Jia G., Keely B., Knappy C., Kondo M., Krishnan S., Lincoln S., Lipp J. S., Mangelsdorf K., Martínez-García A., Ménot G., Mets A., Mollenhauer G., Ohkouchi N., Ossebaar J., Pagani M., Pancost R. D., Pearson E. J., Peterse F., Reichart G.-J., Schaeffer P., Schmitt G., Schwark L., Shah S. R., Smith R. W., Smittenberg R. H., Summons R. E., Takano Y., Talbot H. M., Taylor K. W. R., Tarozo R., Uchida M., van Dongen B. E., Van Mooy B. A. S., Wang J., Warren C., Weijers J. W. H., Werne J. P., Woltering M., Xie S., Yamamoto M., Yang H., Zhang C. L., Zhang Y., Zhao M. and Sinninghe Damsté J. S. (2013b) An interlaboratory study of TEX_{86} and BIT analysis of sediments, extracts, and standard mixtures. *Geochem. Geophys. Geosyst.* **14**, 5263–5285.

Spencer R. G., Hernes P. J., Aufdenkampe A. K., Baker A., Gulliver P., Stubbins A., Aiken G. R., Dyda R. Y., Butler K. D., Mwamba V. L., Mangangu A. M., Wabakanghanzi J. N. and Six J. (2012) An initial investigation into the organic matter biogeochemistry of the Congo River. *Geochim. Cosmochim. Ac*. **84**, 614–627.

Spencer R. G. M., Stubbins A. and Gaillardet J. (2014) Geochemistry of the Congo River, Estuary, and Plume. In *Biogeochemical Dynamics at Large River Coastal Interfaces* (eds. T. S. Bianchi, M. A. Allison and W.-J. Cai). Cambridge University Press, New York, pp. 554–583.

Spencer R. G. M., Hernes P. J., Dinga B. J., Wabakanghanzi J. N., Drake T. W. and Six J. (2016) Origins, seasonality, and fluxes of organic matter in the Congo River. *Global Biogeochem. Cy.* **30**, GB005427.

Spencer-Jones C. L., Wagner T., Dinga B. J., Schefuß E., Mann P. J., Poulsen J. R., Spencer R. G., Wabakanghanzi J. N. and Talbot H. M. (2015) Bacteriohopanepolyols in tropical soils and sediments from the Congo River catchment area. *Org. Geochem*. **89-90**, 1–13.

831 Still C. and Powell J. (2010) Continental-scale distributions of vegetation stable carbon isotope
832 ratios. In *Isoscapes* (eds. J. B. West, G. J. Bowen, T. E. Dawson and K. P. Tu). Springer,
833 New York, pp. 179–194.
834 Stuiver M. and Polach H. A. (1977) Discussion: Reporting of ^{14}C data. *Radiocarbon* **19**, 355–
835 363.
836 Talbot H. M., Handley L., Spencer-Jones C. L., Dinga B. J., Schefuß E., Mann P. J., Poulsen J.
837 R., Spencer R. G., Wabakanghanzi J. N. and Wagner T. (2014) Variability in aerobic
838 methane oxidation over the past 1.2 Myrs recorded in microbial biomarker signatures
839 from Congo fan sediments. *Geochim. Cosmochim. Ac*. **133**, 387–401.
840 Thomas R. J. and Asakawa N. M. (1993) Decomposition of leaf litter from tropical forage
841 grasses and legumes. *Soil Biol. Biochem*. **25**, 1351–1361.
842 Tierney J. E., Russell J. M., Eggermont H., Hopmans E. C., Verschuren D. and Sinninghe
843 Damsté J. S. (2010) Environmental controls on branched tetraether lipid distributions in
844 tropical East African lake sediments. *Geochim. Cosmochim. Ac*. **74**, 4902–4918.
845 Wang Z. A., Spencer R. G., Dinga B. J., Mann P. J., Hoering K. A., Poulsen J. R. and Holmes R.
846 M. (2013) Inorganic carbon speciation and fluxes in the Congo River. *Geophys. Res. Lett.*
847 **40**, 511–516.
848 Weijers J. W. H., Schouten S., van den Donker J. C., Hopmans E. C. and Sinninghe Damsté J. S.
849 (2007) Environmental controls on bacterial tetraether membrane lipid distribution in
850 soils. *Geochim. Cosmochim. Ac*. **71**, 703–713.
851 Weijers J. W. H., Bernhardt B., Peterse F., Werne J. P., Dungait J. A. J., Schouten S. and
852 Sinninghe Damsté J. S. (2011) Absence of seasonal patterns in MBT–CBT indices in
853 mid-latitude soils. *Geochim. Cosmochim. Ac*. **75**, 3179–3190.
854 Whiteside J. H., Eglinton T. I., Olsen P. E., Cornet B., McDonald N. G. and Huber P. (2011)
855 Pangean great lake paleoecology on the cusp of the end-Triassic extinction.
856 *Palaeogeogr., Palaeoclimatol., Palaeoecol*. **301**, 1–17.
857 Zell C. I., Kim J.-H., Abril G., Sobrinho R. L., Dorhout D., Moreira-Turcq P. and Sinninghe
858 Damsté J. S. (2013) Impact of seasonal hydrological variation on the distributions of
859 tetraether lipids along the Amazon River in the central Amazon basin: Implications for
860 the MBT/CBT paleothermometer and the BIT index. *Front. Microbiol*. **4**, 228.

Zell C. I., Kim J.-H., Balsinha M., Dorhout D., Fernandes C., Baas M. and Sinninghe Damsté J. S. (2014) Transport of branched tetraether lipids from the Tagus River basin to the coastal ocean of the Portuguese margin: Consequences for the interpretation of the MBT'/CBT paleothermometer. *Biogeosciences* **11**, 5637–5655.

Zhou L., Tian Y., Myneni R. B., Ciais P., Saatchi S., Liu Y. Y., Piao S., Chen H., Vermote E. F., Song C., and Hwang T. (2014) Widespread decline of Congo rainforest greenness in the past decade. *Nature* **509**, 86-90.

Table and Figure Captions

Table 1: Congo and Oubangui River catchment properties and landcover composition.

Table 2: Matrix of Pearson correlation coefficients (r) and significance p-values for Congo River environmental parameters, POM composition, and GDGT distribution metrics. Statistically significant (p-value ≤ 0.05) correlations are printed in bold.

Table 3: Mixing model end-member compositions. See Discussion S2 for further details.

Table S1: Environmental parameters (Q_w, MAT_{Braz}, T_{riv}, pH_{riv}, [DOC], [POC]) and POM composition (%OC, %TN, $\delta^{13}C$, $\delta^{15}N$, N/C, $\Delta^{14}C$) for all samples presented in this study.

Table S2: Congo River time-series GDGT fractional abundances and distribution metrics (MBT', CBT, GDGT-0/cren).

Table S3: Calculated Congo River and Oubangui River POM time-series end-member fractional contributions.

Table S4: Congo River time-series RDA summary statistics, biplot scores, sample ("site") scores, and response variable ("species") scores.

Figure 1: Congo River Basin showing **(a)** ecosystem landcover (Mayaux et al., 2004) and **(b)** C_3/C_4 landcover (Still and Powell, 2010). Sampling site markers are as follows: black circle, Congo River time-series (Spencer et al., 2016; this study); black base-down triangle, Oubangui River time-series (Bouillon et al., 2012; 2014); white base-up triangle, Congo River ≥ 63 μm POM (Spencer et al., 2012); white bar, Congo River upstream (Marwick et al., 2015); white base-down triangle, Oubangui River downstream (this study); white base-right triangle, Sangha River (this study). For reference, the Oubangui River sub-basin upstream of Bangui Station is outlined with a thick red line.

Figure 2: Environmental parameter time-series plots: **(a)** Congo River discharge (Q_w), **(b)** river water pH (pH_{riv}; Wang et al., 2013), **(c)** DOC concentration ([DOC]), **(d)** POC concentration ([POC]; Hemingway et al., 2016), **(e)** Congo River water temperature (T_{riv}), and **(f)** mean monthly air temperature at Brazzaville/Kinshasa (MAT_{Braz}). Where visible, dark gray envelope is ± 1σ uncertainty and light gray envelope is 95 % confidence interval. Dotted line in panel **(a)** is the 1977 to 2006 (inclusive) average hydrograph (repeated for multiple years; Spencer et al., 2012).

Figure 3: Congo River POM and GDGT time-series plots: **(a)** $\delta^{13}C$, **(b)** $\delta^{15}N$, **(c)** N/C, **(d)** $\Delta^{14}C$, **(e)** MBT', **(f)** CBT, and **(g)** GDGT-0/cren ratio. Where visible, dark gray envelope is ± 1σ uncertainty and light gray envelope is 95 % confidence interval. Horizontal dotted lines are the flux-weighted-average values for each calendar year (January to August only for 2013). Slopes and *p*-values are printed for measurements exhibiting a statistically significant (*p*-value ≤ 0.05) secular trend throughout the time-series. For reference, discharge (Figure 2a) is reprinted here above panel **(a)**.

Figure 4: Conservative tracer mixing model plots showing all published POM data from within the Congo Basin: **(a)** $\delta^{13}C$ vs. N/C and **(b)** $\delta^{13}C$ vs. $\Delta^{14}C$. End-member compositions are listed in Table 3 and described in Discussion S2. Distribution of Cuvette Congolaise peat OM $\Delta^{14}C$ values from Dargie et al. (2017) is additionally shown in panel **(b)** as a violin plot.

Figure 5: Correlations between Congo River and Oubangui River discharge vs. **(a)** $\delta^{13}C$, **(b)** N/C, and **(c)** $\delta^{15}N$. To present both records on the same scale, discharge has been normalized by the median discharge value for each time-series ($Q_w/Q_{w,\ median}$). Regression equations, correlation coefficients (*r*), significance *p*-values, and root mean squared error (RMSE) values are shown for each correlation.

Figure 6: Fractional contribution correlations with discharge and box-and-whisker plots for: **(a)** C_3 soils, **(b)** C_3 vegetation, and **(c)** phytoplankton. To present both records on the same scale, discharge has been normalized by the median discharge value for each time-series ($Q_w/Q_{w,\ median}$). For box-and-whisker plots, gray lines are median values, boxes contain the inter-quartile range,

and whiskers contain the 95 % confidence interval. Individual outliers are plotted as black circles (Congo) or triangles (Oubangui).

Figure 7: Congo River time-series RDA triplot ("Type III" scaling) showing the first (RDA1) and second (RDA2) canonical axes. Environmental variable scores are plotted as black arrows, response variable ("species") scores are plotted as gray dashed arrows, and individual sample ("site") scores are plotted as gray circles. Gray axes and labels correspond to response variable scores and black axes and labels correspond to environmental variable scores.

Figure S1: Core lipid GDGT structures showing both 5-methyl and 6-methyl homologues for branched compounds.

Supplemental Discussion

S1. Effect of 6-methyl brGDGTs

Updated chromatographic methods not employed here now allow for the separation of previously co-eluting 5-methyl and 6-methyl brGDGTs and have led to improved metrics for tracking environmental parameters when calibrated using a global soil dataset (De Jonge et al., 2013; 2014b; Hopmans et al., 2016). However, the tetramethylated brGDGTs (brIa to brIc), which contribute ≥ 80 % of total brGDGTs in all samples presented here (Table S2), exist only as 5-methyl homologues (De Jonge et al., 2013). As such, fractional abundance of 6-methyl compounds only becomes significant at soil pH values greater than ≈ 6 (De Jonge et al., 2014b), suggesting that these homologues are of minimal importance in the highly acidic soils of the Congo Basin.

Indeed, linear regressions of MBT'/CBT and the newly defined MBT'_{5ME}/CBT_{5ME}, which omit 6-methyl compounds, in tropical acidic soils analyzed by De Jonge et al. (2014b) are both statistically identical to the 1:1 line (MBT' vs. MBT'_{5ME}: $r = 0.93$, p-value $= 1.14 \times 10^{-8}$, $n = 19$; CBT vs. CBT_{5ME}: $r = 1.00$, p-value $= 0.0$, $n = 16$; not shown). Additionally, for the samples presented in this study, omission of brIIa and brIIb in equation *(3)* does not introduce any scatter when compared to calculated CBT ($r = 1.00$, p-value ≈ 0.00, root mean square error = 0.008), indicating that the trends observed here are robust and are not significantly affected by co-eluting 5-methyl and 6-methyl homologues.

960

961 S2. End-member compositions

962 Vegetation and soil $\delta^{13}C$ and N/C compositions are estimated using all literature values
963 from tropical rainforest and savanna locations, as data from central Africa are sparse or
964 nonexistent, and are presented in Table 3 (Cleveland and Liptzin, 2007; Diefendorf et al., 2010;
965 Magill et al., 2013; Meyers, 1994; Powers and Schlesinger, 2002a; 2002b; Ross et al., 2002;
966 Thomas and Asakawa, 1993). We note that aquatic macrophytes are a potentially important
967 source of POM, especially when water flux through the Cuvette Congolaise is high. However,
968 Duarte (1992) calculates a macrophyte N/C composition of 0.054 ± 0.019, statistically identical
969 to the C_3 tropical rainforest vegetation end-member value used here (p-value = 2.10×10^{-2}), and
970 Hemingway et al. (2016) show that $\delta^{13}C$ values of plant waxes extracted from Congo River TSS
971 are insensitive to seasonal variability in macrophyte contribution. Our mixing model therefore
972 cannot resolve terrestrial vs. aquatic C_3 tropical rainforest vegetation and combines these within
973 a single end member.

974 In contrast to terrestrial inputs, autochthonous phytoplankton biomass is nitrogen-rich,
975 with a canonical N/C value near 0.15 (Anderson and Sarmiento, 1994). Additionally,
976 phytoplankton utilize DIC as a carbon source with an apparent fractionation ($\Delta\delta^{13}C = \delta^{13}C_{product}$
977 $- \delta^{13}C_{source}$) near -21 ‰ (Rau et al., 1989), leading to highly variable $\delta^{13}C$ values due to
978 seasonality in DIC isotope composition (Bouillon et al., 2014). We confirm that phytoplankton in
979 the Congo basin exhibits canonical N/C and $\Delta\delta^{13}C$ values by plotting Oubangui discharge vs.
980 POC $\delta^{13}C$ (Figure 6a) and N/C (Figure 6b). As discharge approaches zero (*i.e.* when
981 incorporation of allochthonous material would become negligible), regressions point to a
982 phytoplankton end member with $\delta^{13}C$ = (-29.3 ± 0.2) ‰ and N/C = 0.153 ± 0.004, and measured
983 DIC $\delta^{13}C$ values are near -8 ‰ during base-flow conditions (Bouillon et al., 2012). For the
984 Oubangui River, we therefore calculate phytoplankton $\delta^{13}C$ for each sample as the corresponding
985 DIC $\delta^{13}C$ value minus 21 ‰ (Table 3). For the Congo River, DIC $\delta^{13}C$ must be estimated using
986 the observed dependence on pCO_2 (Bouillon et al., 2014) and measured pCO_2 values from Wang
987 et al. (2013). We note that the time-series of Wang et al. (2013) does not cover the years 2012 to
988 2013, and we thus repeat 2011 monthly pCO_2 values for these years (Table 3).

Soil $\Delta^{14}C$ values cannot be constrained *a priori*, preventing the use of radiocarbon content as a conservative tracer within our mixing model. Because we are unaware of any published $\Delta^{14}C$ values for Congo River DIC, we calculate phytoplankton $\Delta^{14}C$ as the average value of atmospheric CO_2 between the years 2010 and 2013 (Graven, 2015). This implicitly assumes a negligible hard-water effect on DIC $\Delta^{14}C$, a reasonable assumption given the extremely low carbonate rock weathering rates (0.017 tC km^{-2} yr^{-1}; Copard et al., 2007), rapid rates of OM remineralization, and large influence of organic acids in determining DIC speciation and concentration in the Congo River (Wang et al., 2013). Additionally, we estimate the $\Delta^{14}C$ values of rainforest and savanna vegetation as the average of coarse (≥ 63 μm) POC reported in Spencer et al. (2012), as this has been shown to contain predominantly vascular plant material and thus tracks the inclusion of bomb-derived ^{14}C into this end member (Table 3).

Supplemental References

Anderson L. A. and Sarmiento J. L. (1994) Redfield ratios of remineralization determined by nutrient data analysis. *Global Biogeochem. Cy*. **8**, 65–80.

Duarte C. M. (1992) Nutrient concentration of aquatic plants: patterns across species. *Limnol. Oceangr.* **37**, 882–889.

Hopmans E. C., Schouten S. and Sinninghe Damsté J. S. (2016) The effect of improved chromatography on GDGT-based palaeoproxies. *Org. Geochem*. **93**, 1–6.

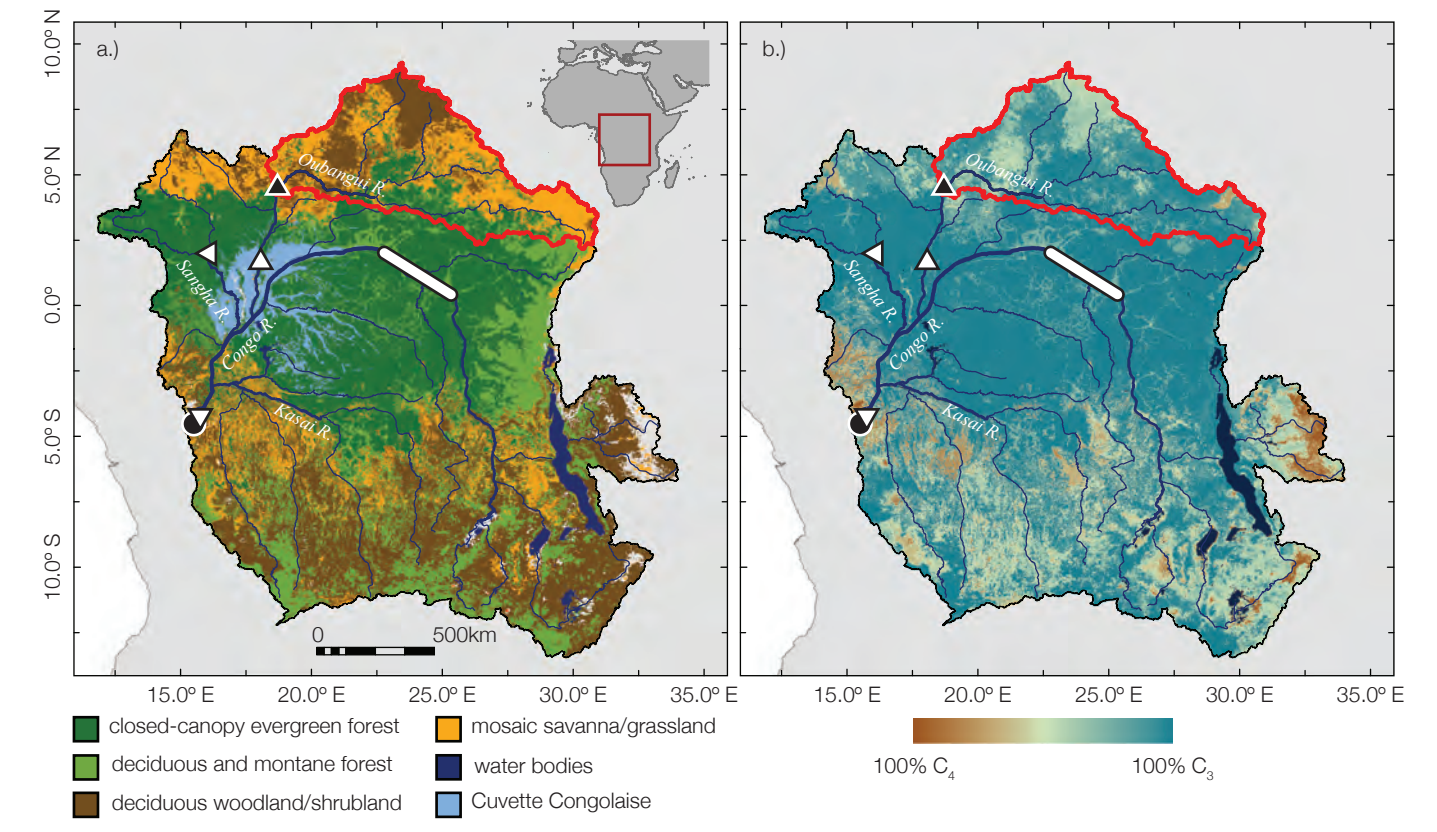
a.)
b.)
Oubangui R.
Sangha R.
Congo R.
Kasai R.
0
500km
10.0° N
5.0° N
0.0°
5.0° S
10.0° S
15.0° E
20.0° E
25.0° E
30.0° E
35.0° E
closed-canopy evergreen forest
deciduous and montane forest
deciduous woodland/shrubland
mosaic savanna/grassland
water bodies
Cuvette Congolaise
100% C_4
100% C_3

a.)
b.)
c.)
d.)
e.)
f.)
Q_w (x1000 m^3 s^{-1})
pH_{riv}
[DOC] (mg L^{-1})
[POC] (mg L^{-1})
T_{riv} (°C)
MAT_{Braz}
Feb '11
Aug '11
Feb '12
Aug'12
Feb '13
Aug '13

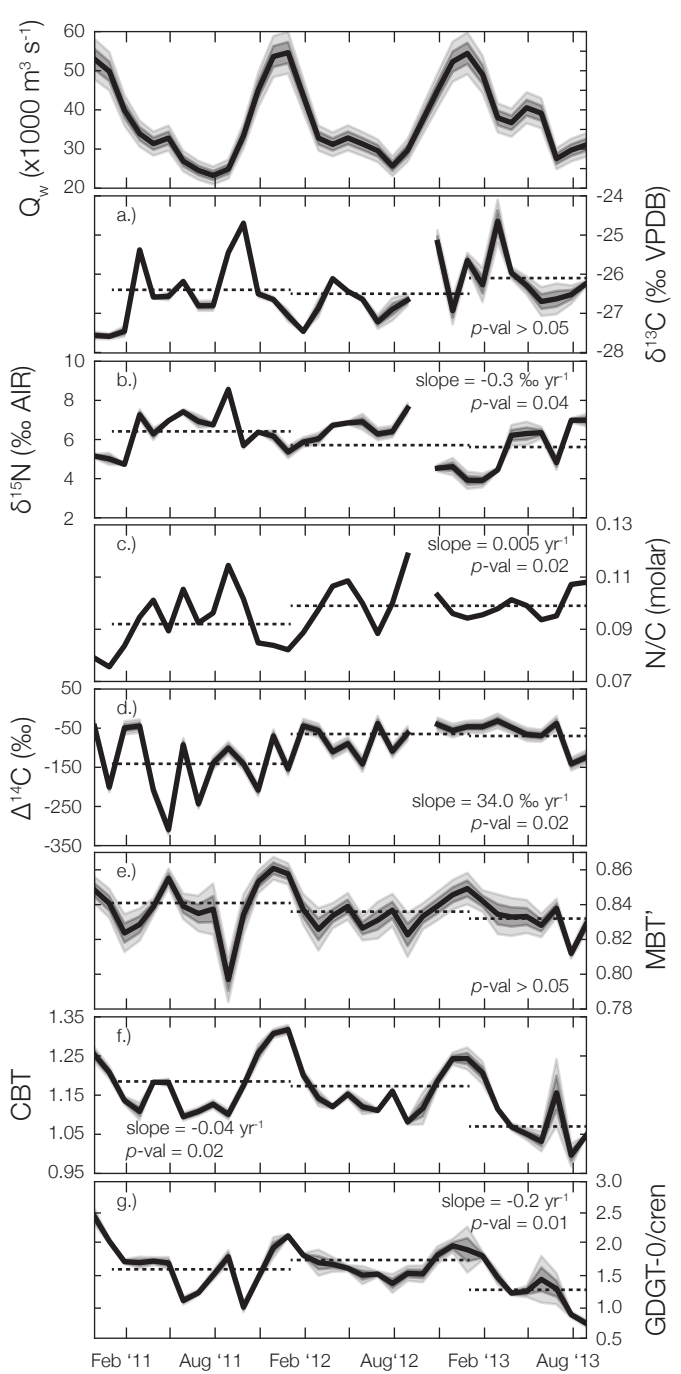
Q_w (x1000 m^3 s^{-1})
60
50
40
30
20
a.)
p-val > 0.05
δ^{13}C (‰ VPDB)
-24
-25
-26
-27
-28
δ^{15}N (‰ AIR)
10
8
6
4
2
b.)
slope = -0.3 ‰ yr^{-1}
p-val = 0.04
c.)
slope = 0.005 yr^{-1}
p-val = 0.02
N/C (molar)
0.13
0.11
0.09
0.07
Δ^{14}C (‰)
50
-50
-150
-250
-350
d.)
slope = 34.0 ‰ yr^{-1}
p-val = 0.02
e.)
p-val > 0.05
MBT'
0.86
0.84
0.82
0.80
0.78
CBT
1.35
1.25
1.15
1.05
0.95
f.)
slope = -0.04 yr^{-1}
p-val = 0.02
g.)
slope = -0.2 yr^{-1}
p-val = 0.01
GDGT-0/cren
3.0
2.5
2.0
1.5
1.0
0.5
Feb '11
Aug '11
Feb '12
Aug'12
Feb '13
Aug '13

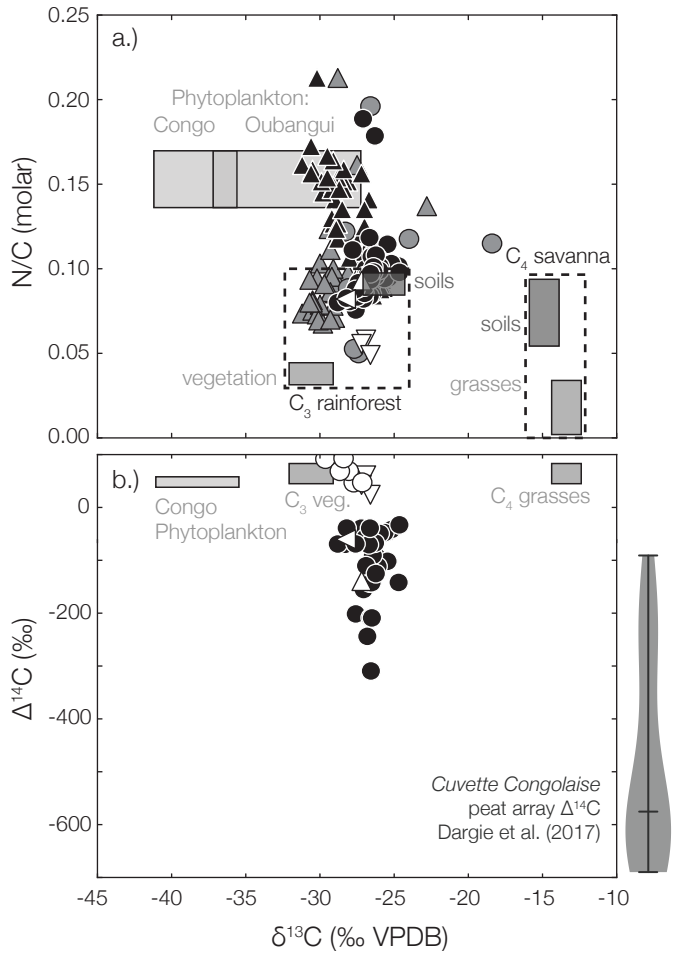

- Congo River at Brazzaville (Mariotti et al., 1991; Spencer et al. 2012; 2016; this study)
- Oubangui River at Bangui (Bouillon et al., 2012; 2014)
- Congo River tributaries (Mariotti et al., 1991)
- Oubangui River tributaries (Bouillon et al., 2014)
- Congo River ≥63 µm POM (Spencer et al., 2012)
- Congo River upstream (Marwick et al., 2015)
- Oubangui River downstream (this study)
- Sangha River (this study)

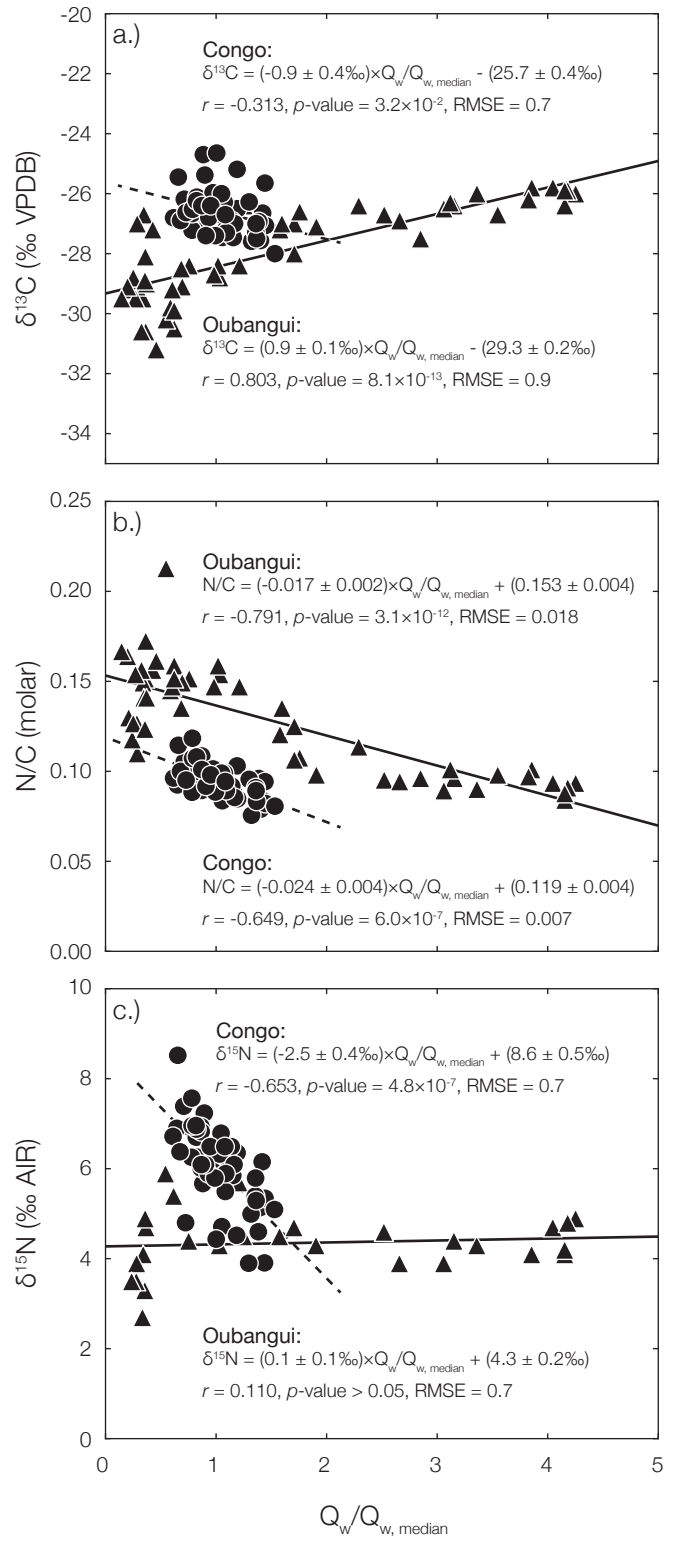
a.)
Congo:
$\delta^{13}C = (-0.9 \pm 0.4‰) \times Q_w/Q_{w,\,median} - (25.7 \pm 0.4‰)$
$r = -0.313$, p-value = 3.2×10^{-2}, RMSE = 0.7
Oubangui:
$\delta^{13}C = (0.9 \pm 0.1‰) \times Q_w/Q_{w,\,median} - (29.3 \pm 0.2‰)$
$r = 0.803$, p-value = 8.1×10^{-13}, RMSE = 0.9
$\delta^{13}C$ (‰ VPDB)
b.)
Oubangui:
$N/C = (-0.017 \pm 0.002) \times Q_w/Q_{w,\,median} + (0.153 \pm 0.004)$
$r = -0.791$, p-value = 3.1×10^{-12}, RMSE = 0.018
Congo:
$N/C = (-0.024 \pm 0.004) \times Q_w/Q_{w,\,median} + (0.119 \pm 0.004)$
$r = -0.649$, p-value = 6.0×10^{-7}, RMSE = 0.007
N/C (molar)
c.)
Congo:
$\delta^{15}N = (-2.5 \pm 0.4‰) \times Q_w/Q_{w,\,median} + (8.6 \pm 0.5‰)$
$r = -0.653$, p-value = 4.8×10^{-7}, RMSE = 0.7
Oubangui:
$\delta^{15}N = (0.1 \pm 0.1‰) \times Q_w/Q_{w,\,median} + (4.3 \pm 0.2‰)$
$r = 0.110$, p-value > 0.05, RMSE = 0.7
$\delta^{15}N$ (‰ AIR)
$Q_w/Q_{w,\,median}$
Congo River at Brazzaville (Spencer et al. 2016; this study)
Oubangui River at Bangui (Bouillon et al., 2012; 2014)

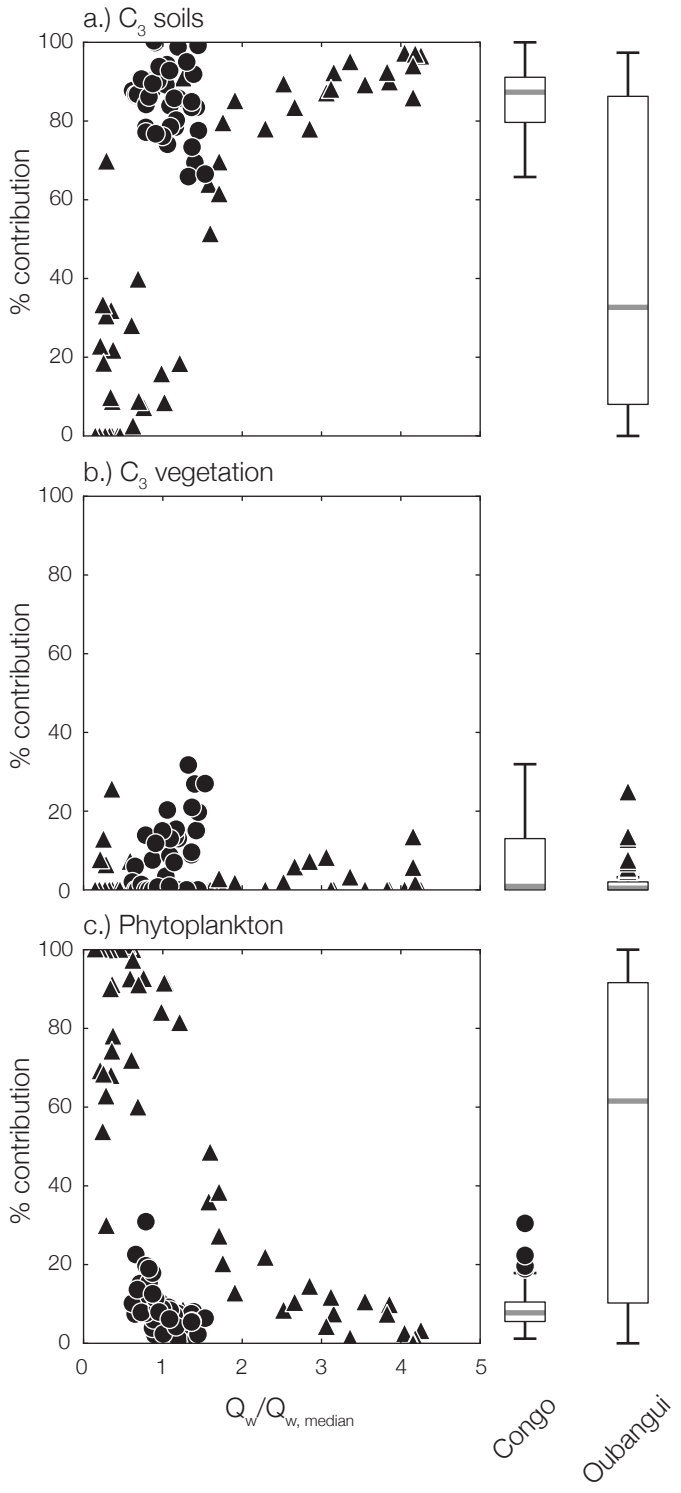

Congo River at Brazzaville (Spencer et al. 2016; this study)

Oubangui River at Bangui (Bouillon et al., 2012; 2014)

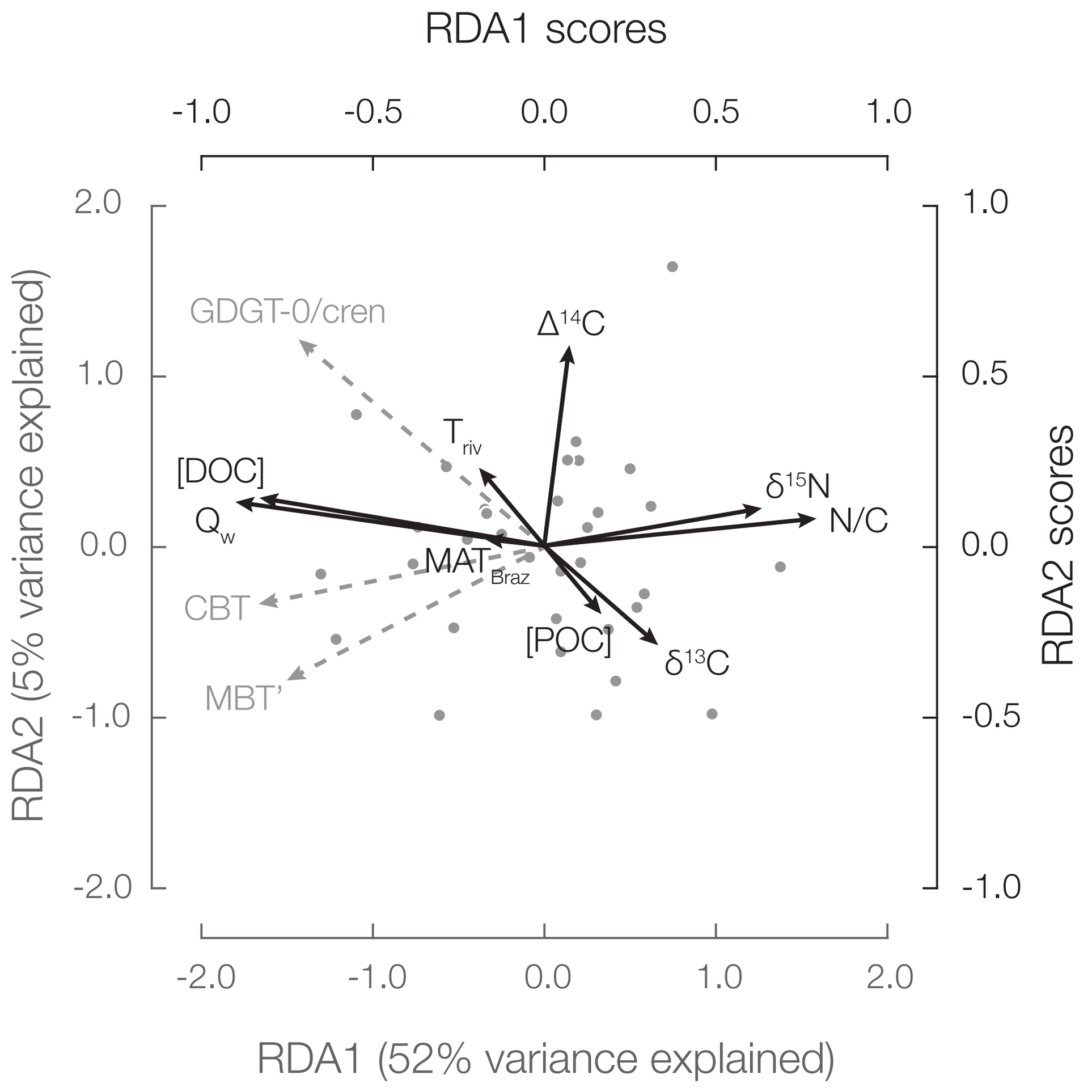
RDA1 scores
-1.0
-0.5
0.0
0.5
1.0
2.0
1.0
0.0
-1.0
-2.0
RDA2 (5% variance explained)
RDA2 scores
GDGT-0/cren
Δ14C
Triv
[DOC]
Qw
δ15N
N/C
MATBraz
CBT
[POC]
δ13C
MBT'
-2.0
-1.0
0.0
1.0
2.0
RDA1 (52% variance explained)

brIa

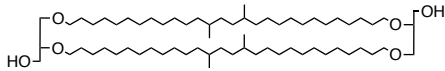

brIb

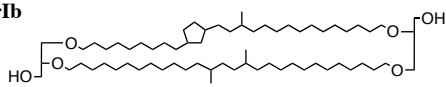

brIc

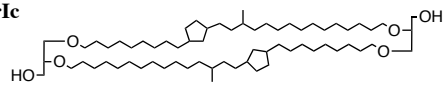

brIIa / brIIa'

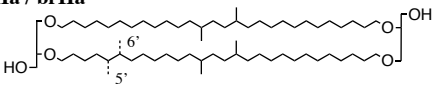

brIIb / brIIb'

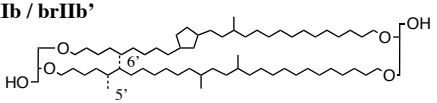

brIIc / brIIc'

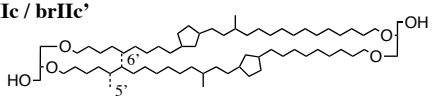

brIIIa / brIIIa'

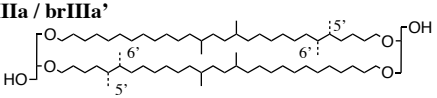

brIIIb / brIIIb'

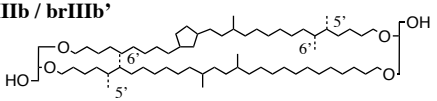

brIIIc / brIIIc'

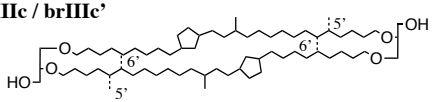

Crenarchaeol

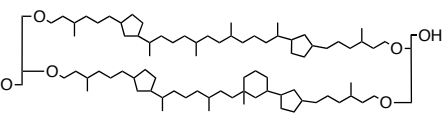

GDGT-0